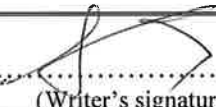




University of  
Stavanger

Faculty of Science and Technology

## MASTER'S THESIS

Study program/ Specialization:  Master degree program in Offshore technology /Marine & Subsea engineering	Spring semester, 2017  Open / <del>Restricted access</del>
Writer: Jeong, Wonmin	 ..... (Writer's signature)
Faculty supervisor: Main supervisor: Muk Chen Ong Co-supervisor : Jasna Bogunovic Jakobsen, Shengnan Liu External supervisor(s):	
Thesis title:  Computational Fluid Dynamics (CFD) simulation of two-dimensional cross sectional flow around twin-box girder bridge	
Credits (ECTS): 30	
Key words: Computational fluid dynamics, CFD Openfoam URANS Twin-box girder bridge Aerodynamics	Pages: 51  + enclosure:  Stavanger, 15.06/2017 Date/year

## Abstract

Flow around a twin-box bridge with a fixed spacing between the decks has been investigated using the two dimensional (2D) Unsteady Reynolds-Averaged Navier–Stokes (URANS) equations with the  $k-\omega$  Shear Stress Transport (SST) turbulence model. Reynolds number ( $Re_D$ ) based on the free stream velocity ( $U$ ) and the bridge deck height ( $D$ ) is about 31,000. Flow characteristics are studied in terms of the flow structures and physics in the range of angle of attack (AoA)  $-10.0^\circ$  to  $+10.2^\circ$ .

The objective of the present study is to evaluate the validity of 2D URANS simulations with  $k-\omega$  SST model for the flow around the twin-box girder bridge. To provide insights for the better bridge design to reduce vortex induced vibration (VIV) in low wind speed, the present study provides CFD study results of aerodynamic factors, force variations and related aerodynamic parameters, for instance, drag coefficient, lift coefficient, moment coefficient and Strouhal number. The formation of the vortices also has been discussed to understand flow characteristic as a function of the angle of attack and how the vortex induced loading may be mitigated.

The drag coefficient, lift coefficient and moment coefficient show a good agreement with the wind tunnel experimental results in the range of AoA  $-10.0^\circ$  to  $+10.2^\circ$ , while the abrupt drop of the lift and moment coefficients are observed at AoA  $+10.2^\circ$ . It is considered that the turbulence modelling is not good enough to capture the flow structure in this high AoA region due to the 3D flow effect.

The Strouhal number is also studied and reported for the engineering design reference purpose. No comparable experimental results are available; thus, further experimental results are required to validate the present study results.

In the meantime, the present study can be useful as an assessment tool for the design of bridges in earlier stage with arbitrary geometries, and for the evaluation of effectiveness of VIV reducing measures like railings, horizontal/vertical stabilizer and all the other arrangements.

## Acknowledgement

This work has been carried out under the supervision of Prof. Muk Chen Ong, Prof. Jasna Bogunovic Jakobsen and PhD candidate Shengnan Liu. I appreciate their guidance with practical advices and continuous encouragement to finish this work.

This research was supported in part with computational resources at NTNU provided by NOTUR, <http://www.sigma2.no>.

This thesis was supported by the Statens vegvesen with Dr. Bjørn Isaksen as the main contract person. I am thankful for the support and interest in the present study.

Last but not least, I would like to thank my wife, Yunkyoung Song for her support and commitment during the course of my study.

# Contents

1	Introduction .....	1
2	Background.....	2
3	OpenFOAM.....	5
3.1	Interpolation Schemes .....	5
3.2	Transient Schemes.....	5
3.3	Solver Algorithm.....	5
3.4	Courant Number.....	6
3.5	Meshing.....	6
4	Turbulence Modelling.....	7
4.1	RANS equations.....	7
4.2	Turbulence models and solvers .....	7
4.3	k- $\omega$ SST model .....	9
4.4	Turbulence profile values .....	10
4.5	Wall functions .....	11
5	Numerical model for CFD study .....	13
5.1	Parameters .....	13
5.2	Boundary Conditions.....	15
5.3	Discretization .....	16
6	CFD analysis result.....	19
6.1	Convergence and Time step sensitivity study.....	19
6.2	Results and discussion.....	22
7	Conclusion.....	38
8	Further Work.....	39
	References.....	40
	Appendix.....	43
A	MATLAB code for the calculation of $C_D$ , $C_L$ , $C_M$ and $St$ .....	43
B	OPENFOAM System files .....	45

# Figures

Figure 1. Section model of the Halsafjorden bridge (Hansen et al. (2016)).....	2
Figure 2: Cross section of the bridge (Hansen et al. (2016)).....	2
Figure 3: Wind tunnel experiment setup (Hansen et al. (2016)).....	3
Figure 4: Log-plot of $u^+$ as a function of $y^+$ . The law of the wall and the log-law are plotted against experimental data to show their regions of validity (Cengel and Cimbala (2010)).....	11
Figure 5: Plot of the lift coefficient over time as it reaches its steady state region of angle of attack $+0.1^\circ$ case.....	14
Figure 6: Initial domain for angle of attack $+0.1^\circ$ case.....	15
Figure 7: Block decomposition of the domain.....	16
Figure 8: Close-up view of block decomposition near to the decks.....	17
Figure 9: Mesh of the full domain of angle of attack $+0.1^\circ$ case.....	17
Figure 10: Close-up of the mesh around the decks of angle of attack $+0.1^\circ$ case.....	18
Figure 11: Drag, lift and moment coefficients for each bridge deck and the sum of decks of angle of attack $+0.1^\circ$ case.....	22
Figure 12: Instantaneous vorticity contour, streamline and pressure coefficient contour plots of angle of attack $+0.1^\circ$ case.....	23
Figure 13: 8 Investigation time instances for the $C_L$ (the sum of the two decks) variation in one period.....	24
Figure 14: Vorticity contour plots from investigation point 1 to point 8 of angle of attack $+0.1^\circ$ case.....	27
Figure 15: Drag, lift and moment coefficients for each bridge deck and the sum of decks of angle of attack $+3.2^\circ$ case.....	28
Figure 16: Drag, lift and moment coefficients for each bridge deck and the sum of decks of angle of attack $+6.3^\circ$ case.....	29
Figure 17: Streamlines of angle of attack $+6.3^\circ$ case.....	30
Figure 18: Streamline of angle of attack $+10.2^\circ$ case.....	30
Figure 19: Drag, lift and moment coefficients for each bridge deck and the sum of decks of angle of attack $-8.1^\circ$ case.....	31
Figure 20: Instantaneous streamlines of angle of attack $-10.0^\circ$ case.....	32
Figure 21: Variation of $\overline{C_D}$ with angle of attack.....	33
Figure 22: Variation of $\overline{C_L}$ with angle of attack.....	33
Figure 23: Variation of $\overline{C_M}$ with angle of attack.....	34
Figure 24 Variation of $St$ with angle of attack.....	34
Figure 25: Variation of the contribution to $C_D$ and $C_L$ of each deck with angle of attack.....	36
Figure 26: Variation of the relative standard deviation of $C_D$ of each deck with angle of attack.....	37

## Tables

Table 1: Boundary conditions for pressure and velocity .....	15
Table 2: Boundary conditions for the turbulence model .....	16
Table 3 : Mesh refinement study showing the null and positive angle of attack, the number of elements, time step and the force parameters with their respective deviation with respect to the results of the finer mesh. ....	19
Table 4: Mesh refinement study showing the negative angle of attack, the number of elements, time step and the force parameters with their respective deviation from the with respect to the results of the finer mesh.....	20
Table 5: The contribution to $C_D$ and $C_L$ with standard deviation of each deck .....	35

## Abbreviations and Symbols

### Abbreviations

RANS	Reynolds Average Navier-Stokes
URANS	Unsteady Reynolds Average Navier-Stokes
CFD	Computational fluid dynamics
PISO	Pressure Implicit Splitting Operators
VIV	Vortex Induced Vibration
LES	Large Eddy Simulation
DNS	Direct Numerical Simulation
DES	Detached Eddy Simulation
FFT	Fast Fourier Transform
CFD	Computational Fluid Dynamics
AoA	Angle of Attack

### Symbols

$k$	Turbulent kinetic energy
$\varepsilon$	Dissipation rate of turbulent kinetic energy
$\omega$	Specific turbulence dissipation rate
$\nu$	Kinematic viscosity
$\nu_t$	Turbulent viscosity
$\rho$	density
$\tau_{ij}$	Reynolds Stress/Turbulent shear stress
$\delta_{ij}$	Kronecker delta
$\bar{u}_i$	Mean velocity
$u_i'$	Fluctuating velocity component
$I$	Turbulent intensity
$E$	Log-law Roughness parameter
$\kappa$	von Karmans constant
$l$	Turbulent length scale
$u_*$	Friction velocity
$u^+$	Non-dimensional flow velocity
$y$	first cell thickness
$y^+$	Non-dimensional first cell thickness
$\tau_w$	Wall shear stress
$St$	Strouhal number
$D$	Bridge deck height
$b$	Bridge deck width
$Re_D$	Reynolds number with respect to bridge height D
$C_L$ or $C_l$	Lift coefficient
$C_D$ or $C_d$	Drag coefficient
$C_M$ or $C_m$	Moment coefficient
$\Delta t$	Time step
$\Delta x$	Cell length
$p$	Mean pressure
$p_0$	Ambient pressure
$f_v$	Vortex shedding frequency
$A_{ref}$	Projected area of the bridge deck
$U$	Inflow velocity
$CFL$	Courant-Friedrichs-Lewy number

# 1 Introduction

This study investigates the two dimensional (2D) flow around a bridge with twin-box girder in the turbulent flow using computational fluid dynamics (CFD). The chosen geometry of the bridge is based on an early design considered for the Halsafjorden bridge, (see the report by Hansen et al (2016)), which is planned along the coastal Highway E39 road in Norway.

First, the main objective of this study is to validate the CFD results with the wind tunnel experimental results and establish general settings with  $k-\omega$  SST turbulence model for this case.  $k-\omega$  SST turbulence model is a popular turbulence model in the external aerodynamic flow simulation for the relatively low Reynolds number. This study establishes the CFD model for the flow around the bridge. The turbulence model is introduced. And the mesh refinement study and time step refinement study are conducted to verify the numerical model.

Secondly, this study compares results of CFD analysis with the wind tunnel experiment results in terms of drag coefficient, lift coefficient, momentum coefficient and Strouhal number. The wind tunnel test was performed with a 1:40 section model by Hansen et al (2016). Among wind tunnel test configurations, we will investigate the case of 0.45 spacing ratio ( $d/b$ ), where  $b$  is 22m for the sum of two decks width and  $d$  is 10 m for the spacing width between the two decks in full scale in the range of AoA  $-10.0^\circ$  to  $+10.2^\circ$ . Calculated Reynolds number is  $Re_D = \frac{UD}{\nu} \cong 3.1 \cdot 10^4$ , where  $U$  is inflow velocity 7.7 m/s,  $\nu$  is kinematic viscosity of the air  $1.51e^{-5} \text{ m}^2\text{s}^{-1}$  and  $D$  is the model deck height 0.0625 m. In this configuration, significant vortex induced vibration were reported in the wind tunnel test.

Finally, this work investigates the flow at each different AoA to provide better understanding to the flow around the bridge decks. The final goal will be to provide a general table for aerodynamic/hydrodynamic properties like drag coefficient, lift coefficient and moment coefficient of each bridge cross section shape in different Reynolds numbers and angles of attack.

In this way the present study can contribute to an improved design of the Halsafjorden bridge and similar types of bridges by providing the insights into the flow-characterization around the bridge decks.

The present study is based on the open source code OpenFOAM, version 3.0.0 and computational resources in NTNU, Vilje.



## 2 Background

Norway has many fjords, and suspension bridge is one of the economic ways to cross the fjords, typically with hundred meters to approximately 1.5 km long in main span. In the present study, so called Halsafjorden bridge which is planned for construction along the E39 road in Norway will be investigated. It is a twin-box girder bridge. The deck height  $h$  is 2.5 m, width  $b$  (the sum of the two decks width) is 22 m and main span length  $L$  is about 2000 m. Figure 1 shows the section model of Halsafjorden bridge and Figure 2 shows the cross section of the bridge, which is our main concern in this study.



Figure 1. Section model of the Halsafjorden bridge (Hansen et al. (2016))

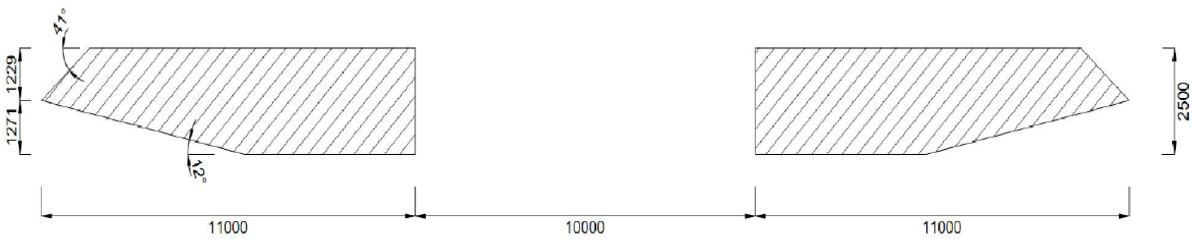


Figure 2: Cross section of the bridge (Hansen et al. (2016))

The wind tunnel experiment with 1:40 scale model of this cross section and  $L$ , the model span of 1.75 m, has been conducted by Hansen et al. (2016). Wind tunnel test schematic is shown in Figure 3.

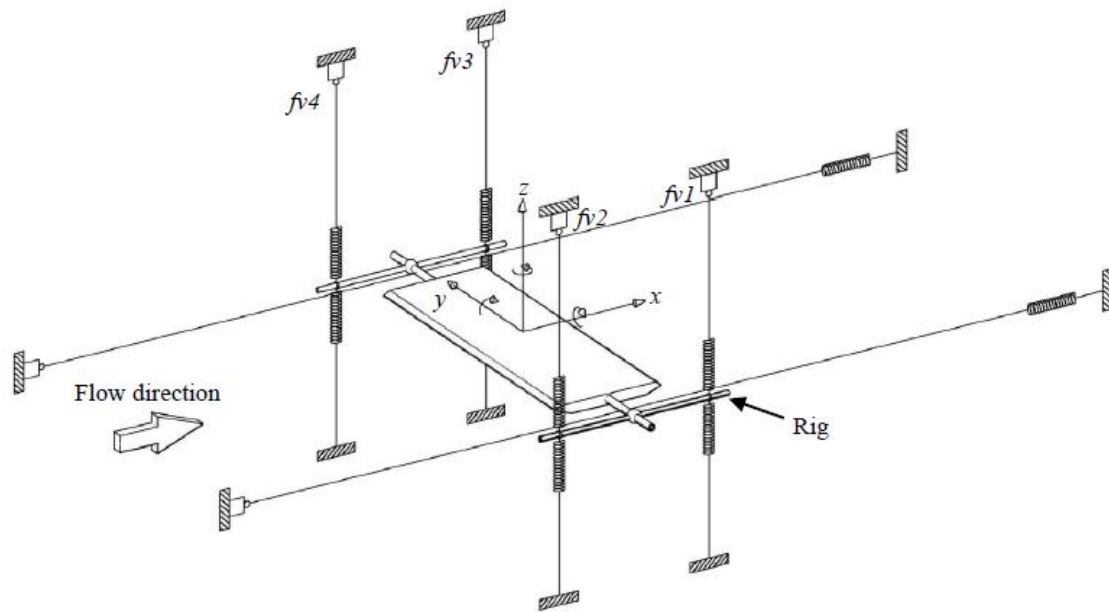


Figure 3: Wind tunnel experiment setup (Hansen et al. (2016))

Denoted  $fv1$  to  $fv4$  are force transducers, which measure forces and thereby the related vertical displacements of the spring ends, so that the vertical and the twisting responses of the model can be deduced. Note that in this wind tunnel experiment, the two decks are connected with 2 beams at each side of the cross section as in Figure 1, so the decks will act as a single deck.

Twin-box bridge decks have favorable aerodynamic properties with respect to flutter stability. On the other hand, this configuration is prone to vortex induced vibration, since vortices shed from the windward box (the first deck in wind direction) can cause important oscillations of the leeward box (the second deck in wind direction) when exciting any natural frequencies of the structure (Sánchez et al. (2015)).

The need for spanning longer distances led to development of such twin-box girder bridge which has an efficient aeroelastic response that girders are more efficient with respect to flutter than their single deck counterparts (Ogawa et al. (2002)). On the other hand, multi-box bridge deck arrangements have shown to be prone to vortex-induced vibrations which must be carefully tackled (Diana et al. (2006)). One of the most important parameters influencing the aerodynamic and aeroelastic response of twin-box decks is the gap distance between the two decks. Focused on studying the effect of the gap width, several experimental works, such as Qin et al. (2009) have been published. The present will study a fixed gap distance which is used in the wind tunnel experiment (Hansen et al. (2016)). The previously mentioned references emphasize the complexity of the flow around the twin-box girder and the dramatic effect of the gap width in the aerodynamic response. It is clear that studying the gap width effect through the wind tunnel experiments is technically complex and requires substantial resources in terms of funding, time and facilities. Moreover, only a limited number of gap widths, geometries, angles of attack and Reynolds numbers can be tested.

A twin-box girder bridge can be simplified as two rectangular decks. Schewe and Larsen (1998) has shown Reynolds number effects in the flow around a bluff bridge deck cross section. They figured out that a bridge with sharp edges can suffer Reynolds number effect which means the aerodynamic parameters change with Reynolds number. Therefore, it is recommended to study behavior of the bridge in a broad range of Reynolds number, while the present study is limited to the fixed Reynolds number which is used in the wind tunnel experiment.

CFD based simulations have shown their potential in wind engineering based design of the bridge decks by Nieto et al. (2008 and 2010). They investigated the Messina strait bridge and the Great belt bridge to study the capability of relatively inexpensive 2D URANS simulations to identify the changes in the aerodynamic parameters ( $C_D$ ,  $C_L$ ,  $C_M$  and  $St$ ) of the given geometries.

The main goal of the present research is to provide general model to study the overall aerodynamic performance of the numerical bridge model while changing parameters. In this work the numerical simulations will be validated with the experimental results reported in Hansen et al. (2016). Therefore, the deck geometry, the gap distance between the two decks and the domain size which are same as in the wind tunnel test will be considered.

Finally, the potential of the 2D URANS models to correctly reproduce the wind tunnel test results in terms of the force coefficients and the vortex shedding characterization of the twin-box decks will be studied. Thus, this study can help at the initial or early design stage of the bridge by providing information for the improved design of the bridge deck configurations: Gap widths, VIV mitigating devices locations, stabilizers and all the other arrangements.

## 3 OpenFOAM

OpenFOAM is an open source CFD software written in C++. It offers a large range of solvers and applications in order to fulfil many needs of the related industry. OpenFOAM is a finite volume solver. That means that the domain is discretized into individual control volumes, and the conservation equations for each cell is found directly from the integral conservation. The alternative would have been a finite difference solver. It uses the partial differential equations (PDEs) of the conservation integral as the base of the computations and therefore treats the discretization as nodes instead of finite volumes. Both methods are applicable for CFD analysis, however the finite volume method is perhaps more common for the commercial codes. OpenFOAM uses a co-located mesh arrangement meaning that all flow values are assigned to the center of the cells. This is different from most other commercial CFD software which uses a staggered type of arrangement, normally assigning the pressure value to the cell center and the velocities to the cell faces.

### 3.1 Interpolation Schemes

Regardless the finite volume or the finite difference method being used, the flow parameter value at a given cell will be an interpolation of the values on the neighboring cells. OpenFOAM offers a number of different interpolation schemes. The two most common are arguably the first order upwind scheme and the central difference scheme. For this analysis the central difference scheme has been chosen. It can be obtained by doing a forward and backward Taylor expansion of the desired quantity and combining the two solutions to get accurate up to the second order expression for both the first and second derivative of the quantities.

### 3.2 Transient Schemes

In order to reach convergence a transient method is applied. For this study the Crank-Nicolson method is applied. The method is a combination of the first order forward and backward Euler method, so that the average of the two is used for better accuracy and calculation speed. It is second order accurate in time and unconditionally stable. However, oscillatory solutions may occur for larger time steps (Ferziger and Peric (2002)). In this context, a time step sensitivity study has been performed.

### 3.3 Solver Algorithm

The Navier-Stokes equations are being solved using the PISO (pressure-implicit split-operator) algorithm. It is an iterative transient solver for incompressible flows. There are no theoretical independent pressure equations to determine the unknown pressure term in the Navier-Stokes equations so initial values must be approximated and then corrected. The PISO algorithm has been assigned to do two pressure corrections (*nCorrectors*), and for each pressure correction perform three non-orthogonal corrections (*nNonOrthogonalCorrectors*) to correct for the non-orthogonality of the mesh (Appendix B, OpenFOAM system files).

### 3.4 Courant Number

When dealing with numerical schemes where the convection plays the dominant role, one of the most pronounced criteria in OpenFOAM is the Courant number (or CFL(Courant-Friedrichs-Lewy) number). It is expressed as:

$$CFL = \frac{u\Delta t}{\Delta x} \quad (3.1)$$

where  $u$  is magnitude of velocity,  $\Delta t$  is time step and  $\Delta x$  is interval length of the cell. The Courant criterion states that this number must be less or equal to one ( $CFL \leq 1$ ). The logic behind this statement is that the time step  $\Delta t$  used in the numerical scheme must be less than the time it takes for the flow to cross one cell length  $\Delta x$ , meaning  $t \leq x/u$ . For our implicit Crank-Nicolson scheme the maximum limit for the time step is less straight forward and more case dependent (Ferziger and Peric (2002)), but for the sake of consistency effort will be made to keep the value below 0.7

### 3.5 Meshing

The meshing is performed in GMSH (Geuzaine and Remacle (2009)). For meshing in general there are some quality aspects that must be fulfilled in order to obtain good results from the simulations. All cell values, except those assigned boundary conditions, are obtained through interpolation of the neighboring cells using a finite difference scheme. This is then run through a number of time steps until a stable solution is reached. This dependency between the cell values means that in an ideal situation you want all the neighboring cells to have the same geometry and size as the cell you are currently obtaining a value for. If size and geometry deviates significantly you risk obtaining a faulty averaged value which then affects the next iterations.

There are many measures of mesh quality. For a quadrilateral mesh there are in general three basic factors to quantify the quality of the mesh. They are the skewness, smoothness and aspect ratio. The skewness is based on how the corner angles of a cell deviates from a  $90^\circ$  angle. The aspect ratio is the ratio between the height and width of a cell where the value of one ensures a quadratic cell, and the smoothness ensures that the transition between the cells is somewhat smooth. For the aspect ratio, we will consider only X-Y domain aspect ratio since the present study is 2D case. Y-Z, X-Z aspect ratio will not be covered. Another important mesh quality indicator is the non-orthogonality, meaning how the normal vector of a cell face deviates from the vector between the cell centers (Mavriplis (1996)).

OpenFOAM has a quality limit regarding generated meshes which must be satisfied in order to run the simulations. This quality check is launched through the *CheckMesh*-command within the working directory, and will provide information regarding the mentioned quality indicators.

Every case in the present study has been checked with *CheckMesh* and no errors were found.

## 4 Turbulence Modelling

### 4.1 RANS equations

The two governing equations being solved by any CFD solver, when excluding heat transfer, are the continuity equation and the Navier-Stokes equations. For incompressible flow these are expressed as (4.1) and (4.2), respectively.

$$\frac{\partial u_j}{\partial x_j} = 0 \quad (4.1)$$

$$\rho \left( \frac{\partial u_i}{\partial t} + u_j \frac{\partial u_i}{\partial x_j} \right) = -\frac{\partial p}{\partial x_i} + \frac{\partial}{\partial x_j} \left( \mu \left[ \frac{\partial u_i}{\partial x_j} + \frac{\partial u_j}{\partial x_i} \right] \right) \quad (4.2)$$

where  $u_i = [u, v, w]$  and  $x_i = [x, y, z]$ .

For turbulent flows, each velocity component consists of one mean velocity and one fluctuating velocity:

$$u_i = \bar{u}_i + u_i' \quad (4.3)$$

Inserting (4.3) into (4.2) and time averaging the result we get the Navier-Stokes equation for turbulent flow, popularly referred to as the Reynolds-Averaged Navier-Stokes (RANS) equations:

$$\rho \left( \frac{\partial \bar{u}_i}{\partial t} + \frac{\partial (\bar{u}_i \bar{u}_j)}{\partial x_j} \right) = -\frac{\partial \bar{p}}{\partial x_i} + \frac{\partial}{\partial x_j} \left( \mu \left[ \frac{\partial \bar{u}_i}{\partial x_j} + \frac{\partial \bar{u}_j}{\partial x_i} \right] - \overline{\rho u_i' u_j'} \right) \quad (4.4)$$

The Reynolds stress is not a physical value, but a result of the time averaging process. There is no direct way of calculating the Reynolds stress, but one way to deal with it is through the use of the Boussinesq approximation in (4.5).

$$\tau_{ij} = \mu_t \left( \frac{\partial \bar{u}_i}{\partial x_j} + \frac{\partial \bar{u}_j}{\partial x_i} \right) - \frac{2}{3} \rho k \delta_{ij} \quad (4.5)$$

In (4.5),  $\mu_t$  is the turbulent eddy viscosity,  $k$  is the turbulent kinetic energy and  $\delta$  is the Kronecker delta. However, we are left with a new unknown, namely the turbulent eddy viscosity  $\mu_t$ . Lots of the different turbulence models evolve around solving for this unknown parameter (Schmitt (2007)).

### 4.2 Turbulence models and solvers

There are several different turbulence models. A large portion of them evolves around solving the RANS equations by introducing different approaches for handling the closure problem with the Reynolds stresses. The largest group of these models are the two-equation models which to a large extent uses the Boussinesq approximation and solves the closure problem by introducing two additional solvable conservation equations (Holmemo (2015)).

It is also possible to solve the RANS equations without using the Boussinesq approximation. The Reynolds Stress Transport models is based on solving conservation equations for the Reynolds Stresses

directly. However, this is more complex than the regular two equations models.

The RANS equations are simplified models to solve the Navier-Stokes equations with time-averaging. It is possible to solve the Navier-Stokes equations without time-averaging. The method is then called DNS (Direct Numerical Simulation) and is done by solving the fluctuating velocity part fully of (4.3) instead of averaging it out. Now we are no longer talking about turbulence models, but actually solving the turbulence. In order to capture the small scale of velocity fluctuations in the flow this method requires a very fine grid resolution and therefore it is very computationally expensive.

Other hybrid methods have evolved from the DNS approach. LES (Large Eddy Simulation) is less computational demanding, where the large-scale eddies are computed and the small scale eddies are modeled using a subgrid-scale model. This is still an expensive approach, but less expensive than the pure DNS.

A hybrid method of the LES is the DES (Detached Eddy Simulation). This approach uses the LES as the standard solver, but is pre-modelled to use the RANS equations near walls or other regions where the fluctuations are somewhat prevented from occurring by the presence of the body surfaces. This saves computational time since near wall regions require the finest grid resolution. There are two popular extensions of this model, namely the DDES (Delayed Detached Eddy Simulation) and the IDDES (Improved Delayed Detached Eddy Simulation). The main difference is the handling of the LES/RANS transitions (Holmemo (2015)).

### 4.3 k- $\omega$ SST model

k- $\omega$  SST turbulence model is a blending model of the k- $\omega$  model and the k- $\varepsilon$  model. The standard k- $\omega$  model is based on the model by Wilcox (1988), which incorporates modifications for low-Reynolds number effects, compressibility and shear flow spreading. The Wilcox model predicts free shear flow spreading rates that are in close agreement with the measurements for far wakes, mixing layers and plane, round, and radial jets, and is thus applicable to wall-bounded flows and free shear flows. A variation of the standard model called the SST model is also available. The SST model was developed by Menter (1994) to effectively blend the robust and accurate formulation of the model in the near-wall region with the free-stream independence of the model in the far field. To achieve this, the model is converted into a formulation, it works as the k- $\omega$  model at near to the walls and as the k- $\varepsilon$  model in the far away from the wall. The SST model is similar to the standard model, but includes some refinements (Tian et al. (2013)). These features make the SST model more accurate and reliable for a class of flows (for example, adverse pressure gradient flows, airfoils, transonic shock waves etc.) than the standard model. The k- $\omega$  SST turbulence model is governed by:

$$\frac{D\rho k}{Dt} = \tau_{ij} \frac{\partial u_i}{\partial x_j} + \beta^* \rho \omega k + \frac{\partial}{\partial x_j} [(\mu + \sigma_k \mu_t) \frac{\partial k}{\partial x_j}] \quad (4.6)$$

$$\frac{D\rho \omega}{Dt} = \frac{\gamma}{\nu_t} \tau_{ij} \frac{\partial u_i}{\partial x_j} - \beta \rho \omega^2 + \frac{\partial}{\partial x_j} [(\mu + \sigma_\omega \mu_t) \frac{\partial \omega}{\partial x_j}] + 2\rho(1 - F_1)\sigma_\omega \frac{1}{\omega} \frac{\partial k}{\partial x_j} \frac{\partial \omega}{\partial x_j} \quad (4.7)$$

where  $\beta^* = \varepsilon/k\omega$  and the turbulence stress tensor is:

$$\tau_{ij} = -\overline{\rho u_i' u_j'} = \mu_t \left( \frac{\partial u_i}{\partial x_j} + \frac{\partial u_j}{\partial x_i} - \frac{2}{3} \frac{\partial u_k}{\partial x_k} \delta_{ij} \right) - \frac{2}{3} \rho k \delta_{ij} \quad (4.8)$$

The turbulence viscosity can be estimated by:

$$\nu_t = \frac{a_1 k}{\max(a_1 \omega, \Omega F_2)} \quad (4.9)$$

Where  $\Omega$  is the absolute value of the vorticity,  $a_1=0.31$  and the function  $F_2$  is given by:

$$F_2 = \tanh \left[ \max \left( \frac{2\sqrt{k}}{0.09\omega y}, \frac{500\nu}{y^2\omega} \right) \right]^2 \quad (4.10)$$

where  $y$  is the distance to the nearest surface or boundary.

The coefficients  $\beta, \gamma, \sigma_k$  and  $\sigma_\omega$  are defined as functions of the coefficients of the k- $\omega$  and k- $\varepsilon$  turbulence models and they are listed as follow:

$$\beta = F_1 \beta_1 + (1 - F_1) \beta_2 \quad \gamma = F_1 \gamma_1 + (1 - F_1) \gamma_2 \quad (4.11)$$

$$\sigma_k = F_1 \sigma_{k1} + (1 - F_1) \sigma_{k2} \quad (4.12)$$

$$\sigma_\omega = F_1 \sigma_{\omega 1} + (1 - F_1) \sigma_{\omega 2} \quad (4.13)$$



where the function  $F_1$  is:

$$F_1 = \tanh \left\{ \left[ \min \left[ \max \left( \frac{2\sqrt{k}}{0.09\omega y}, \frac{500\nu}{y^2\omega} \right), \frac{4\rho\sigma_{\omega 2}k}{CD_{k\omega}y^2} \right] \right]^4 \right\} \quad (4.14)$$

and the coefficient  $CD_{k\omega}$  is:

$$CD_{k\omega} = \max \left( 2\rho\sigma_{\omega 2} \frac{1}{\omega} \frac{\partial k}{\partial x_j} \frac{\partial \omega}{\partial x_j}, 10^{-20} \right) \quad (4.15)$$

the empirical constants of the  $k - \omega$  SST model are (Menter (1994)):

$$\beta^* = 0.09, \beta_1 = 0.075, \beta_2 = 0.0828, \gamma_1 = 0.5532, \gamma_2 = 0.4404, \sigma_{k1} = 0.85, \sigma_{k2} = 1.0, \sigma_{\omega 1} = 0.5 \text{ and } \sigma_{\omega 2} = 0.856.$$

and previous study Nieto et al. (2008 and 2010) has shown that the  $k-\omega$  SST turbulence model is suitable for the external aerodynamic flow around the bridges.

#### 4.4 Turbulence profile values

In OpenFOAM the use of the  $k - \omega$  SST model requires initial values for both the turbulent kinetic energy  $k$ , the specific turbulence dissipation rate  $\omega$  and the turbulent viscosity  $\nu_t$ . The turbulent kinetic energy can be expressed as (4.16):

$$k = \frac{1}{2} \cdot (\overline{u'^2} + \overline{v'^2} + \overline{w'^2}) \quad (4.16)$$

If we assume an isotropic turbulence field, meaning that the fluctuations in all directions are equal, then (4.17) is simplified to:

$$k = \frac{3}{2} \cdot (\overline{u'^2}) \quad (4.17)$$

The term  $\overline{u'^2}$  is still unknown so instead we set it as a fraction of the inflow velocity and it is called that fraction for the turbulent intensity. Hence, (4.17) is transformed to (4.18):

$$k = \frac{1}{2} \cdot [(UI_u)^2 + (UI_v)^2 + (UI_w)^2] \quad (4.18)$$

where  $I$  denotes the turbulent intensity and  $U$  is the inflow velocity. For the present study the horizontal turbulent intensity is set to 12 % and vertical turbulent intensity is set to 8 % as reported in Hansen et al. (2016).

There are several explicit expressions for an initial value for the specific turbulence dissipation rate  $\omega$ . What they all have in common is that they are based on a turbulent length scale  $l$ . The turbulent length scale can be defined in several ways and is one of the reasons why the expression for  $\omega$  deviates between authors. For our purpose we use the following expression as (4.19) which were used in Tian et al. (2013),

$$\omega = \frac{C_\mu^{-\frac{1}{4}} k^{\frac{1}{2}}}{l} \quad (4.19)$$

where  $l$  is the turbulent length scale set equal to 7 % of the body height, i.e.  $0.07D$ , and  $C_\mu$  is set to 0.09. The turbulent viscosity  $\nu_t$  has relationship with  $k$  and  $\omega$  and is expressed as:

$$\nu_t = \frac{k}{\omega} \quad (4.20)$$

#### 4.5 Wall functions

In turbulent flow the boundary layer can be said to be decomposed into four regions. Closest to the wall the flow will be laminar and viscous effects will dominate the flow characteristics. This layer is called the viscous sublayer. A little further from the wall turbulent effects will be present, but viscous effects are still dominant. This is the buffer layer. After the buffer layer turbulent effects becomes dominant over the viscous and we call the layer as overlap layer. Then, far enough from the wall the flow will be more or less unaffected by the presence of the wall and we move into the fully turbulent region of the flow. The different regions are illustrated in Figure 4.

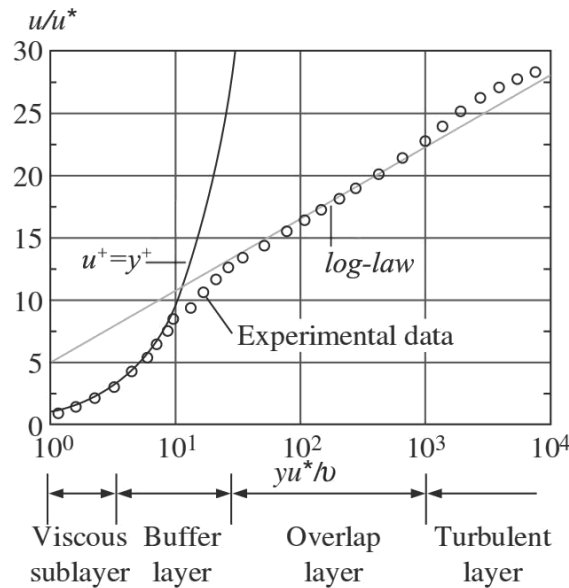


Figure 4: Log-plot of  $u^+$  as a function of  $y^+$ . The law of the wall and the log-law are plotted against experimental data to show their regions of validity (Cengel and Cimbala (2010))

One of the popular turbulence models for the engineering purposes is the standard  $k-\epsilon$  model, which is only valid for fully turbulent flow, meaning high Reynolds number region. The presence of a no-slip wall introduces local low Reynolds number regions close to the wall in which the standard  $k-\epsilon$  is not valid due to the dominating viscous effects. The solution to this problem is to introduce so called wall functions. These are semi-empirical formulas that give an approximation of the boundary layer where the viscous effects are present, without the need to numerically solve these regions. This is beneficial both because the solution becomes more accurate due to the  $k-\epsilon$  equations actually being valid, but also because it saves computational costs due to less grid refinement needed near the wall.

But this wall function approach is mainly for high Reynolds number region. In the present study, Reynolds number is  $Re_D = 3.1 \cdot 10^4$ , which is considered as relatively low Reynolds number region, so that wall function approach may not be valid. Nieto et al. (2008) showed that applying the wall function approach is questionable in the similar cases.

In the  $k$ - $\omega$  SST turbulence model, the boundary layer can be calculated without wall function, instead with the given boundary conditions (Nieto et al. (2008)). For the accurate results, it is important to calculate viscous sublayer, which has high effects on drag and lift forces. In our simulations, omega boundary condition is given by ‘*fixedValue*’ not by ‘*omegaWallFunction*’.

For the wall of the two decks,  $k$  and  $\omega$  boundary conditions are given as:

$$k \approx 0 \quad (4.21)$$

$$\omega = \frac{60\nu}{\beta_1(\Delta y_1)^2} \quad (4.22)$$

Theoretically,  $k = 0$  at the wall, but this may cause error in CFD calculations, since some terms are divided with  $k$  in the process so it will cause floating error. Instead very small number (ex:  $1e^{-12}$ ) can be used. And  $\omega$  has a large value at the wall, where  $\beta_1 = 0.075$ , and  $\Delta y_1$  is normal distance to next node from the wall surface (Tian et al. (2013)).

The non-dimensional wall distance  $y^+$  can be expressed as:

$$y^+ = \frac{hu^*}{\nu} \quad (4.23)$$

Where  $h$  is distance from the wall surface to nearest node,  $u^*$  is called the friction velocity given by  $u^* = \sqrt{\frac{\tau_w}{\rho}}$ .  $y^+$  value should be reasonable around the wall to calculate viscous layer accurately. Average  $y^+$  value of 1 to 5 along the wall is recommended for this.

## 5 Numerical model for CFD study

### 5.1 Parameters

This section is meant to give a description of the main study parameters being used throughout this work.

The Reynolds number is based on the deck height  $D$  of the bridge deck (see Figure 6) and is hence expressed as:

$$Re_D = \frac{UD}{\nu} \quad (5.1)$$

where  $U$  is the inflow velocity,  $D$  is the height of the bridge and  $\nu$  is the viscosity of the fluid. In the present study, the Reynolds number used for the wind tunnel experiment test will be used.

The main results of interest are the drag coefficient, lift coefficient, moment coefficient and Strouhal number. Averaged pressure coefficient over the bridge decks will also be considered. The drag, lift and moment coefficients are defined below:

$$C_D = \frac{F_{drag}}{\frac{1}{2}\rho U^2 D} \quad (5.2)$$

$$C_L = \frac{F_{lift}}{\frac{1}{2}\rho U^2 b} \quad (5.3)$$

$$C_M = \frac{F_{moment}}{\frac{1}{2}\rho U^2 b^2} \quad (5.4)$$

where  $\rho$  is the density of the fluid,  $U$  is the inflow velocity,  $D$  is the bridge height and  $b$  is the bridge width, and these parameters are used to normalize the coefficients. For the  $C_M$  calculation, the shear center refers to the center of the spacing between the decks in both X and Y axis.

The Strouhal number is the vortex shedding frequency  $f_v$  made non-dimensional parameter with respect to the deck height  $D$  and the inflow velocity  $U$  as (5.5):

$$St = \frac{Df_v}{U} \quad (5.5)$$

The averaged pressure coefficient is expressed as (5.6):

$$C_p = \frac{\bar{p} - p_0}{\frac{1}{2}\rho U^2} \quad (5.6)$$

where  $\bar{p}$  = static pressure or local pressure,  $p_0$  = freestream pressure.

All the parameters are calculated with results data after the stabilized time. Figure 5 shows example of  $C_L$  plot after the stabilized time, where there is no significant change of parameters trend in a continued simulation process.

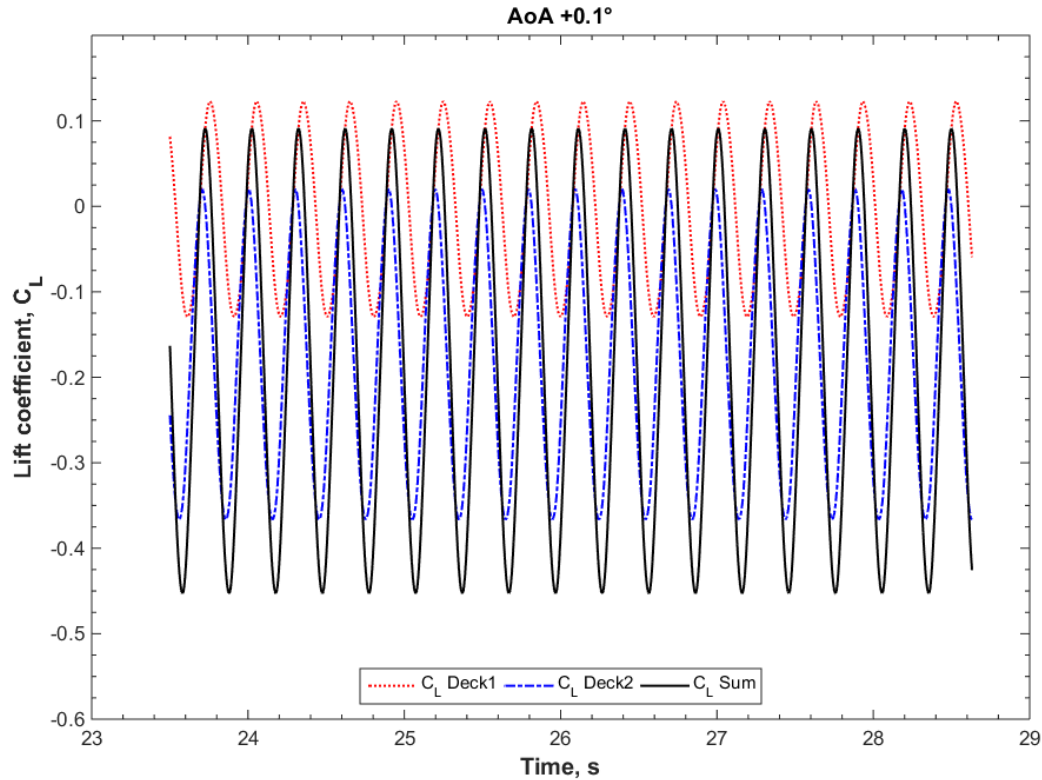


Figure 5: Plot of the lift coefficient over time as it reaches its steady state region of angle of attack  $+0.1^\circ$  case

The mean drag, lift and moment coefficients are found by averaging the coefficients over a representative number of periods.

Unlike typical cases of flow around cylinder, root mean square of the lift coefficient will not be used. This is because the bridge deck has an asymmetric cross section; thus, the average of the lift coefficient will not be zero over the time. The standard deviation of each deck will be studied to understand the flow physics around the decks as function of AoA.

The Strouhal number is found by making a periodogram of the lift coefficient, by using the Fast Fourier Transform (FFT). The sampling frequency is calculated from the time step  $\Delta t$  as applied in the simulations. Fourier transform will be used to figure out the dominant frequency of the lift coefficient, that is our  $f_v$ , vortex frequency.

In the wind tunnel experiment report (Hansen et al. (2016)) Strouhal numbers for the vortex induced vibration tests are available. But in the present study, we are using static coefficient test conditions for the simulations, so no direct comparable Strouhal numbers are available. For the further analysis and the reference, the predicted Strouhal numbers in the present study will be reported in Section 6.

## 5.2 Boundary Conditions

Figure 6 shows the domain surfaces with their corresponding names and dimensions. The configuration from the wind tunnel test has been used, the bridge deck model size (1:40) and the CFD domain size in Y direction is same as the wind tunnel. Some reasonable assumptions are made to define the domain: the length from the inlet to the center of the spacing between the decks in X direction is set to  $18.8D$  and the length from the center of the spacing between the decks to the outlet in X direction is set to  $77.2D$ , to reduce or remove the domain effect.

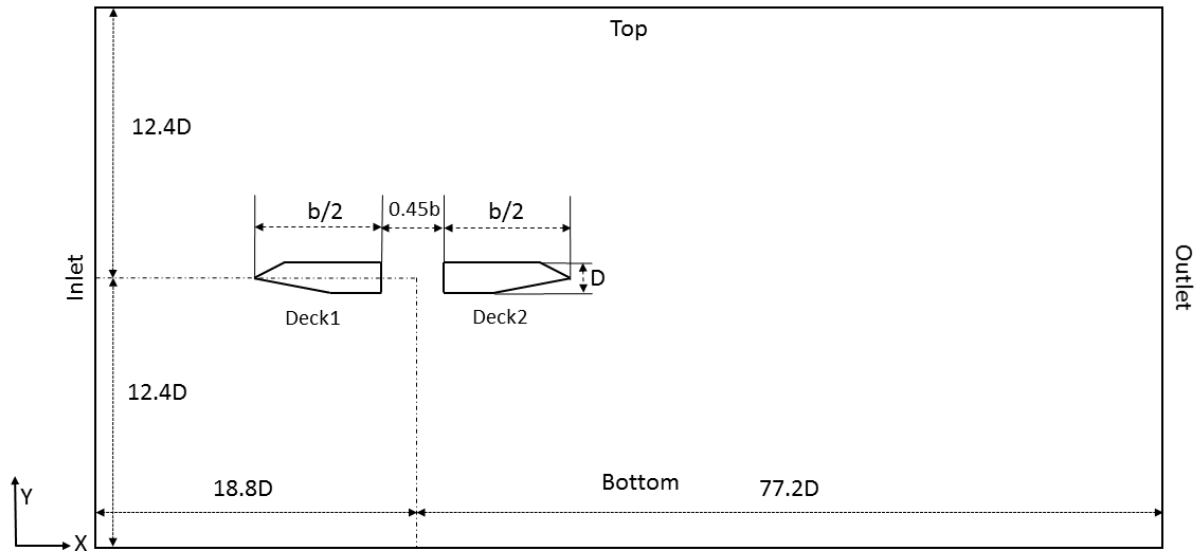


Figure 6: Initial domain for angle of attack  $+0.1^\circ$  case

The boundary conditions for the flow velocity and pressure are displayed in table 1.

Table 1: Boundary conditions for pressure and velocity

Location	p	U
<i>Deck1/Deck2</i>	zeroGradient	fixedValue
<i>Inlet</i>	zeroGradient	fixedValue
<i>Outlet</i>	fixedValue	zeroGradient
<i>Top</i>	zeroGradient	fixedValue
<i>Bottom</i>	zeroGradient	fixedValue

'ZeroGradient' means that the gradient of any parameter is zero at the boundary. For the pressure that means no change in the direction normal to the surface,  $\partial p / \partial n = 0$ . Similarly, for the velocity the zero gradient boundary condition means  $\partial \mathbf{u} / \partial n = 0$  at the boundary, where  $\mathbf{u} = [u, v, w]$ . 'Fixed value' of zero for the velocity at the surface of the decks corresponds to the no-slip condition, and at the inlet the velocity is set to normalized value to the positive x-direction.

The *Top* and *Bottom* surfaces are set to 'ZeroGradient' meaning that the normal gradient of any scalar quantity, and the vectors themselves normal to the surface, are zero.

OpenFOAM only accepts 3D meshes meaning two additional surfaces in z-axis are added by default and assigned the boundary condition ‘empty’. This will ensure a 2D flow through the 3D domain.

In addition, when using the  $k-\omega$  SST model it is required to assign boundary conditions for  $k$ ,  $\omega$  and  $v_t$ . These boundary conditions are needed to give the flow the right turbulence profile within the bounds of the turbulence model. They can be found according to Section 4.4 and are displayed in Table 2. These values are calculated from normalized inlet velocity  $U=1$  m/s to the positive X direction.

The present study uses same domain size in Y direction as in the wind tunnel test for the CFD simulations. Usually in 2D simulations, the *Top* and *Bottom* boundary conditions are set to ‘zeroGradient’ and it is reasonable for the analysis. In the present study, setting ‘zeroGradient’ at the *Top* and *Bottom* boundaries from the initial simulation time yielded the divergence of the solution. To stabilize the simulations, at the initial stage of the simulation the *Top* and *Bottom* boundary conditions are set as the wall, where is  $k=0$ ,  $\omega=$  the calculated value from equation (4.22),  $p=$ ‘zeroGradient’ and  $U=$ ‘fixedValue’ (0,0,0). After the stabilization, the  $\omega$  is set to ‘zeroGradient’, where this trick helped the convergence of the simulations.

Table 2: Boundary conditions for the turbulence model

Location	$k$	$\omega$	$v_t$
<i>Inlet</i>	$1.04 \cdot 10^{-2}$	42.557	calculated
<i>Outlet</i>	zeroGradient	zeroGradient	calculated
<i>Top</i>	fixedValue	zeroGradient	calculated
<i>Bottom</i>	fixedValue	zeroGradient	calculated
<i>Deck1/Deck2</i>	0 (or $1 \cdot 10^{-12}$ )	276851	calculated

### 5.3 Discretization

For the better control of the discretization process, the domain was partitioned into several blocks as shown in Figure 7 with GMSH. A closer view of the block closest to the decks is depicted in Figure 8. The red bold lines illustrate the two decks of the bridge.



Figure 7: Block decomposition of the domain

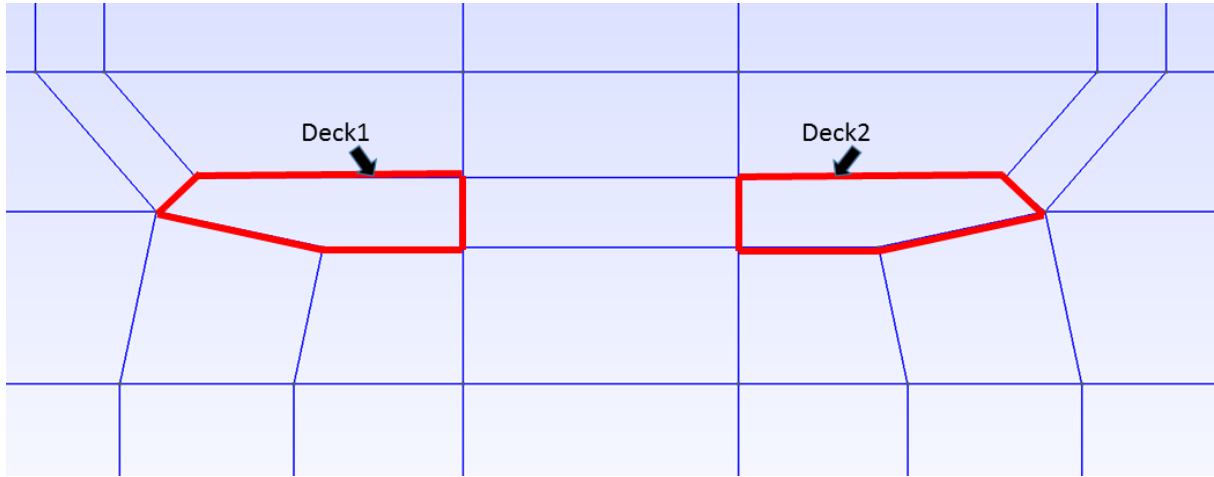


Figure 8: Close-up view of block decomposition near to the decks

With the block configuration shown in Figure 7 and 8, the mesh around the decks is displayed in Figure 9 and 10. The mesh is composed exclusively of structured quadrilateral elements with a refined boundary layer mesh closest to the body surfaces (Figure 10).

When proceeding with the simulations the results appeared to be sensitive in mesh quality and methodology. Attention to the mesh quality was required to assure stable calculation, and different meshing approaches are used for the different AoA cases.

With more meshes, we have more accurate results but it should be compromised between the accuracy and computational resources. So the convergence study has been performed in this context in Section 6.

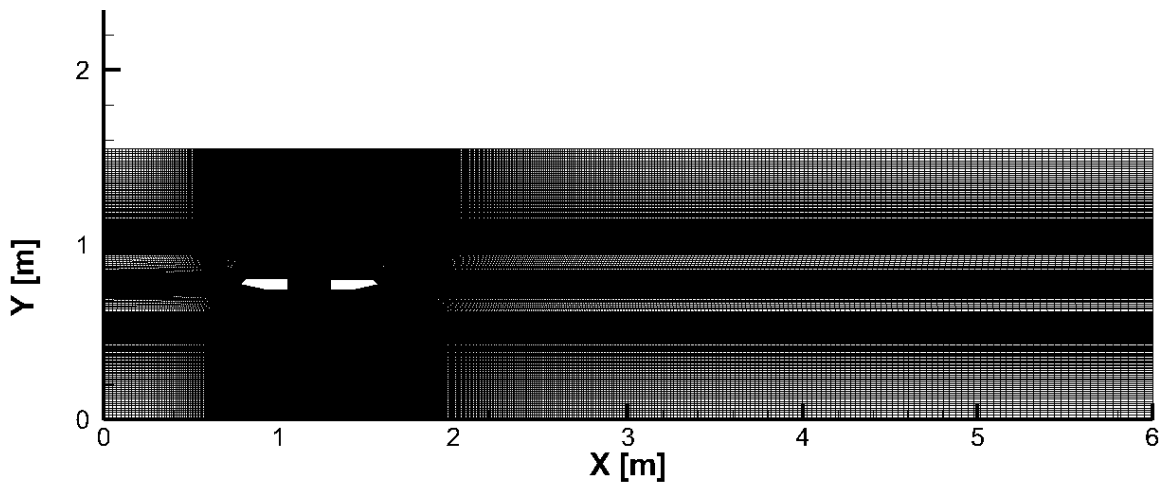


Figure 9: Mesh of the full domain of angle of attack  $+ 0.1^\circ$  case



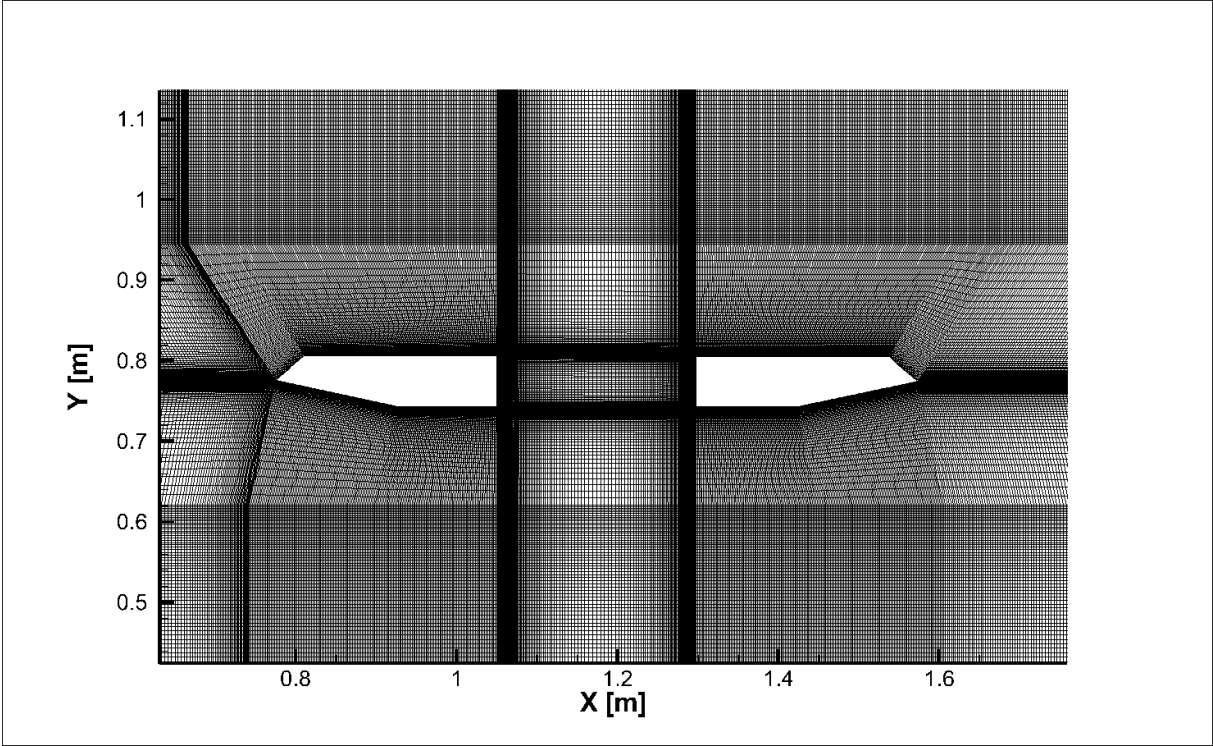


Figure 10: Close-up of the mesh around the decks of angle of attack  $+ 0.1^\circ$  case

## 6 CFD analysis result

### 6.1 Convergence and Time step sensitivity study

A mesh refinement study is performed under the same domain decomposition and mesh resolution, but under the different meshing methodology. Table 3 and 4 shows the number of elements and their respective values for the drag coefficient, lift coefficient, moment coefficient and Strouhal number. In addition, the relative percentage in the results with respect to the finer mesh are shown.

Table 3 : Mesh refinement study showing the null and positive angle of attack, the number of elements, time step and the force parameters and the St numbers with their respective deviation with respect to the results of the finer mesh.

AoA <sup>o</sup>	Case	Elements	$\Delta t$ (s)	$\overline{C_D}$	$\overline{C_L}$	$\overline{C_M}$	St	% $\overline{C_D}$	% $\overline{C_L}$	% $\overline{C_M}$	% St
0.1	M1	138354	5.00E-05	1.164	-0.154	0.077	0.224	-	-	-	-
0.1	M2	198834	5.00E-05	1.129	-0.176	0.078	0.216	-3.0	-14.0	1.3	-3.7
0.1	M3*	288034	5.00E-05	1.125	-0.178	0.075	0.216	-0.3	-1.7	-2.8	0.0
0.1	M3T1	288034	2.50E-05	1.142	-0.180	0.082	0.225	1.5	-0.6	8.2	4.3
1.5	M1	138354	5.00E-05	1.088	-0.051	0.127	0.203	-	-	-	-
1.5	M2	198834	5.00E-05	1.096	-0.057	0.125	0.201	0.7	-12.3	-1.8	-0.7
1.5	M3*	288034	5.00E-05	1.099	-0.057	0.123	0.205	0.2	-0.7	-1.8	2.0
1.5	M3T1	288034	2.50E-05	1.114	-0.047	0.126	0.196	1.4	18.2	2.2	-4.4
3.2	M1	138354	5.00E-05	1.080	0.141	0.182	0.201	-	-	-	-
3.2	M2	198834	5.00E-05	1.087	0.160	0.181	0.191	0.7	14.0	-0.5	-5.1
3.2	M3*	288034	5.00E-05	1.091	0.154	0.180	0.192	0.3	-3.8	-0.8	0.4
3.2	M3T1	288034	2.50E-05	1.101	0.147	0.180	0.200	1.0	-5.0	-0.2	4.4
4.4	M1	138354	5.00E-05	1.106	0.245	0.218	0.186	-	-	-	-
4.4	M2*	288034	5.00E-05	1.106	0.228	0.210	0.192	0.0	-6.8	-3.8	3.4
4.4	M3	545954	5.00E-05	1.083	0.238	0.211	0.200	-2.1	4.1	0.7	4.0
4.4	M3T1	545954	2.50E-05	1.112	0.241	0.211	0.196	2.7	1.5	-0.1	-2.2
6.3	M1	138354	2.50E-05	1.429	0.260	0.177	0.261	-	-	-	-
6.3	M2*	288034	2.50E-05	1.111	0.313	0.235	0.250	-22.3	20.4	32.7	-4.1
6.3	M3	545954	2.50E-05	1.096	0.313	0.239	0.240	-1.4	0.0	1.5	-3.9
6.3	M3T1	545954	1.25E-05	1.107	0.325	0.240	0.244	1.0	3.7	0.5	1.6
8.1	M1	138354	2.50E-05	1.820	0.338	0.207	0.126	-	-	-	-
8.1	M2	198834	2.50E-05	1.654	0.371	0.202	0.136	-9.1	9.8	-2.4	8.5
8.1	M3*	288034	2.50E-05	1.628	0.387	0.206	0.142	-1.6	4.4	2.0	4.2
8.1	M3T1	288034	1.25E-05	1.636	0.395	0.207	0.137	0.5	2.0	0.7	-3.3
10.2	M1	198834	2.50E-05	2.045	0.263	0.148	0.125	-	-	-	-
10.2	M2	272914	2.50E-05	2.037	0.210	0.141	0.107	-0.4	-20.1	-5.0	-14.6
10.2	M3*	362514	2.50E-05	2.039	0.208	0.132	0.110	0.1	-1.0	-5.8	2.8
10.2	M3T1	362514	1.25E-05	2.057	0.200	0.130	0.101	0.9	-4.0	-1.8	-7.9

\* Selected case for further study

Table 4: Mesh refinement study showing the negative angle of attack, the number of elements, time step and the force parameters and the St numbers with their respective deviation from the with respect to the results of the finer mesh

AoA°	Case	Elements	$\Delta t$ (s)	$\overline{C_D}$	$\overline{C_L}$	$\overline{C_M}$	St	% $\overline{C_D}$	% $\overline{C_L}$	% $\overline{C_M}$	% St
-1.4	M1	138354	5.00E-05	1.277	-0.190	0.024	0.228	-	-	-	-
-1.4	M2	198834	5.00E-05	1.230	-0.208	0.020	0.214	-3.7	-9.2	13.6	-6.3
-1.4	M3*	288034	5.00E-05	1.230	-0.209	0.019	0.217	0.0	-0.7	4.9	1.5
-1.4	M3T1	288034	2.50E-05	1.205	-0.210	0.024	0.211	-2.0	-0.3	-22.2	-2.7
-2.9	M1	138354	5.00E-05	1.345	-0.208	-0.053	0.226	-	-	-	-
-2.9	M2	198834	5.00E-05	1.339	-0.207	-0.038	0.218	-0.5	0.0	27.2	-3.8
-2.9	M3*	288034	5.00E-05	1.340	-0.200	-0.038	0.220	0.1	3.7	1.0	1.0
-2.9	M3T1	288034	2.50E-05	1.318	-0.191	-0.039	0.226	-1.6	4.6	-2.6	2.6
-4.0	M1	138354	5.00E-05	1.512	-0.251	-0.080	0.212	-	-	-	-
-4.0	M2	198834	5.00E-05	1.482	-0.219	-0.066	0.215	-2.0	12.9	17.2	1.3
-4.0	M3*	288034	5.00E-05	1.487	-0.217	-0.066	0.212	0.4	0.9	0.6	-1.5
-4.0	M3T1	288034	2.50E-05	1.485	-0.216	-0.065	0.213	-0.1	0.2	0.9	0.4
-6.2	M1	138354	5.00E-05	1.512	-0.354	-0.165	0.203	-	-	-	-
-6.2	M2	198834	5.00E-05	1.517	-0.362	-0.163	0.196	0.3	-2.3	-1.5	-3.6
-6.2	M3*	288034	5.00E-05	1.519	-0.364	-0.163	0.198	0.1	-0.6	0.1	1.2
-6.2	M3T1	288034	2.50E-05	1.512	-0.381	-0.161	0.203	-0.5	-4.6	-0.8	2.1
-8.1	M1	138354	1.25E-05	2.094	-0.681	-0.181	0.160	-	-	-	-
-8.1	M2	198834	1.25E-05	1.963	-0.653	-0.188	0.180	-6.3	4.2	3.5	12.8
-8.1	M3*	288034	1.25E-05	2.023	-0.664	-0.182	0.182	3.1	-1.8	-3.3	1.1
-8.1	M3T1	288034	6.25E-06	2.064	-0.649	-0.191	0.176	2.0	2.2	5.3	-3.2
-10.0	M1	138354	2.50E-05	2.567	-0.793	-0.135	0.182	-	-	-	-
-10.0	M2	198834	2.50E-05	2.473	-0.733	-0.185	0.100	3.6	7.6	37.1	-45.1
-10.0	M3*	288034	2.50E-05	2.526	-0.733	-0.176	0.104	-2.2	-0.1	-5.1	4.0
-10.0	M3T1	288034	1.25E-05	2.507	-0.727	-0.173	0.095	0.7	0.9	-1.8	-8.9

\* Selected case for further study

All cases have average  $y^+$  value from 1.2 to 3.1 for the both decks. To control the  $y^+$  value different meshing methodologies were used for the different angle of attack cases.

In every angle of attack case, the convergence study has been performed until the relative deviation is less than 5 %. For AoA  $+0.1^\circ$ ,  $+1.5^\circ$ ,  $+10.2^\circ$ ,  $-1.5^\circ$ ,  $-8.1^\circ$  and  $-10.0^\circ$  cases there are relative deviation values more than 5 %, but the absolute change difference is less than or equal to 0.01 which can be considered as the differences are in acceptable criteria.

Drag coefficient and Strouhal number have less independence on element numbers while lift and moment coefficients are more sensitive with the element numbers and the meshing methodology.

As the decks decline, there is higher acceleration when the flow passing by the corners of the decks. So to keep the CFL number below 0.7, at higher angle of attack cases which have the angle amplitude larger than 6, a reduced time step 2.5E-5 s is used for the study.

Especially for AoA  $-8.1^\circ$  case, with the time step of 2.5E-5 s, M3 case satisfied the criteria for the mesh

refinement study but there is relatively big lift difference more than 10 % between M3T1 case with the time step  $1.25E-5$  s and M3 case with time step  $2.5E-5$  s. Thus reduced time step  $1.25E-5$  s is used for the following mesh refinement study. Unlike other cases, AoA  $-8.1^\circ$  and  $-10.0^\circ$  showed chaotic behavior in the coefficients. In the present study the effort was put into the calculations of the coefficients in these two cases to reduce the calculation error by averaging the values in long time.

Through the convergence study, it can be concluded that the mesh resolution and the time step for each angle of attack case that selected for further study can give sufficient accuracy.

## 6.2 Results and discussion

Figure 11 shows  $C_D$ ,  $C_L$  and  $C_M$  versus AoA of AoA  $+0.1^\circ$  case respectively, and Figure 12 shows instantaneous vorticity contour, streamline and pressure coefficient contour plots of angle of attack  $+0.1^\circ$  case.

By interpreting the plots like Figure 11 and Figure 12, we can understand flow characteristics and physics of each angle of attack case. Here we discuss AoA  $+0.1^\circ$  case in detail, other cases can be studied in same manner.

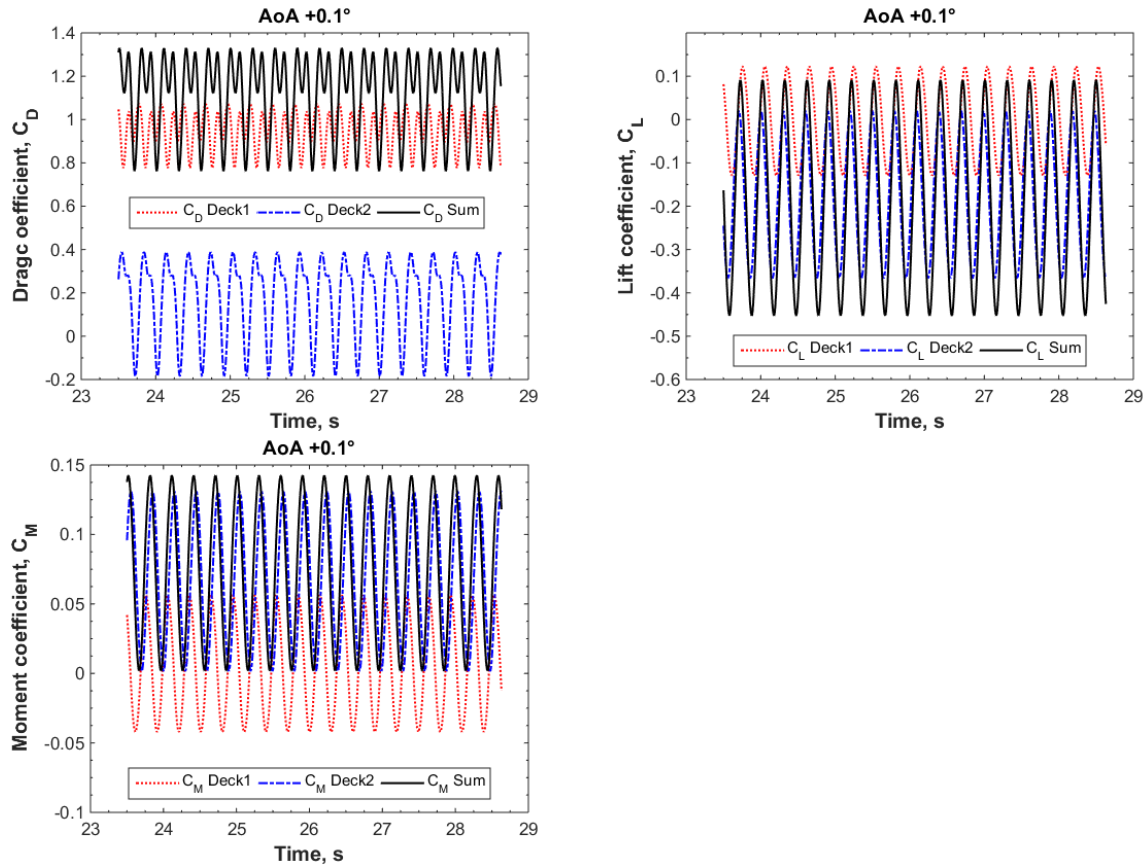


Figure 11: Drag, lift and moment coefficients for each bridge deck and the sum of decks of angle of attack  $+0.1^\circ$  case

For AoA  $+0.1^\circ$  case, the combined drag coefficient, the sum of the two decks drag coefficients, has two peaks in one period while both lift and moment coefficient have one peak per one period. Because the vortices, see Figure 12 vorticity plot, which are generated at the windward downstream vertical edge attack the leeward deck, one vortex is generated from the upper surface of the windward deck and the other from the lower surface of the windward deck, the asymmetric geometry generates different size of vortices which cause drag force fluctuation at the leeward deck. The vorticity contour plot in Figure 12 shows that the vortices which are generated from the windward deck while the lower vortex is about to detach and to attack the leeward deck.

The streamline plot in Figure 12 also can provide insight of the flow structure. The recirculating bubble is created at the downstream vertical edge of the windward deck and the vortex rotation direction is periodically changing over the time.

So VIV mitigating devices and measures should reduce these vortices generation or should block these vortices attack to the leeward deck. Railings and stabilizers can be the candidates for the VIV suppression.

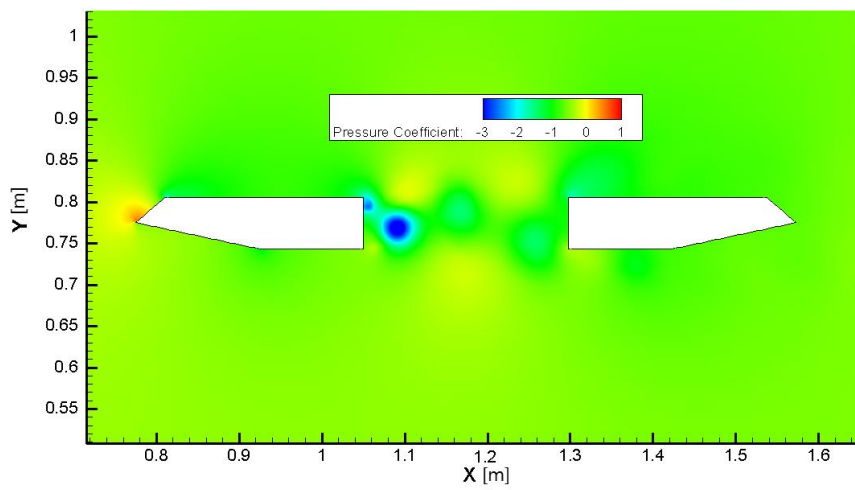
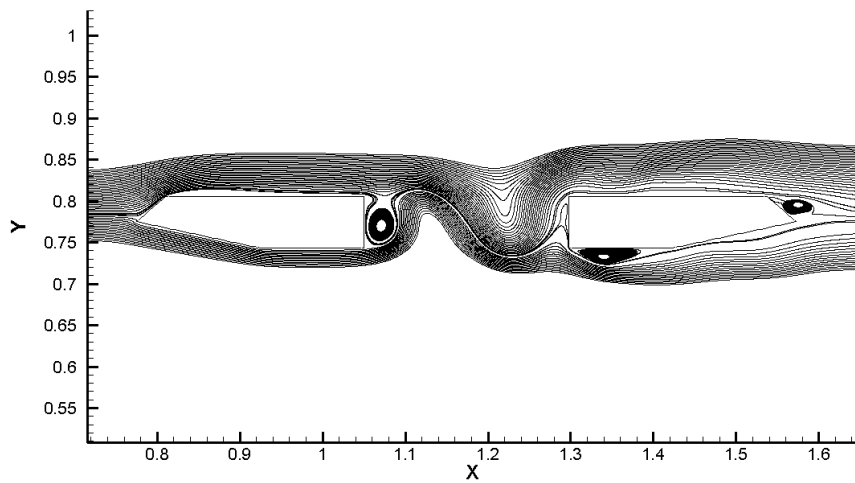
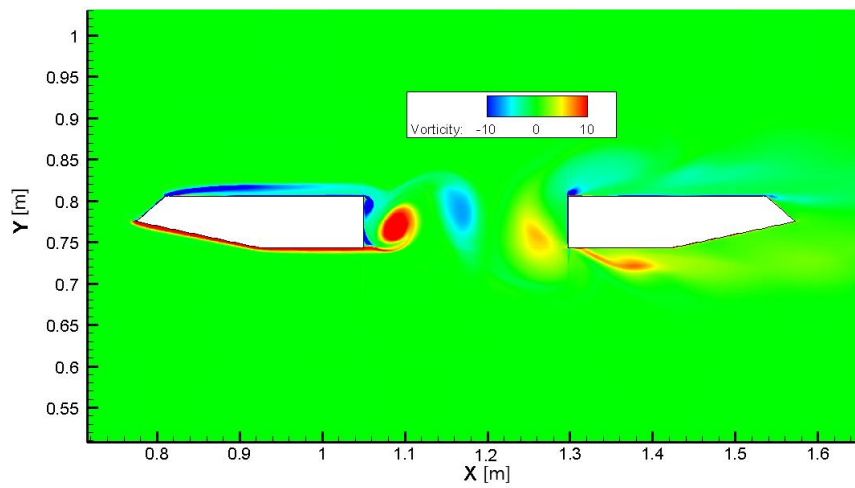


Figure 12: Instantaneous vorticity contour, streamline and pressure coefficient contour plots of angle of attack  $+0.1^\circ$  case

One of our main concerns is VIV behavior of the bridge. To investigate this, arbitrary one  $C_L$  period was sampled after the stabilized time and one period is divided into 8 investigation time instances. Time instance 1 indicates where the  $C_L$  is maximum and time instance 5 indicates minimum. From maximum to minimum, the  $C_L$  axis is divided by 3 lines, one is mean crossing line, one mid-line between maximum and mean crossing line and one mid-line between minimum and mean crossing line. This  $C_L$  is for the sum of the two decks not for the either of each deck. Note that it takes slightly longer time from time instance 1 to time instance 5 than from time instance 5 to next  $C_L$  peak due to the asymmetric geometry.

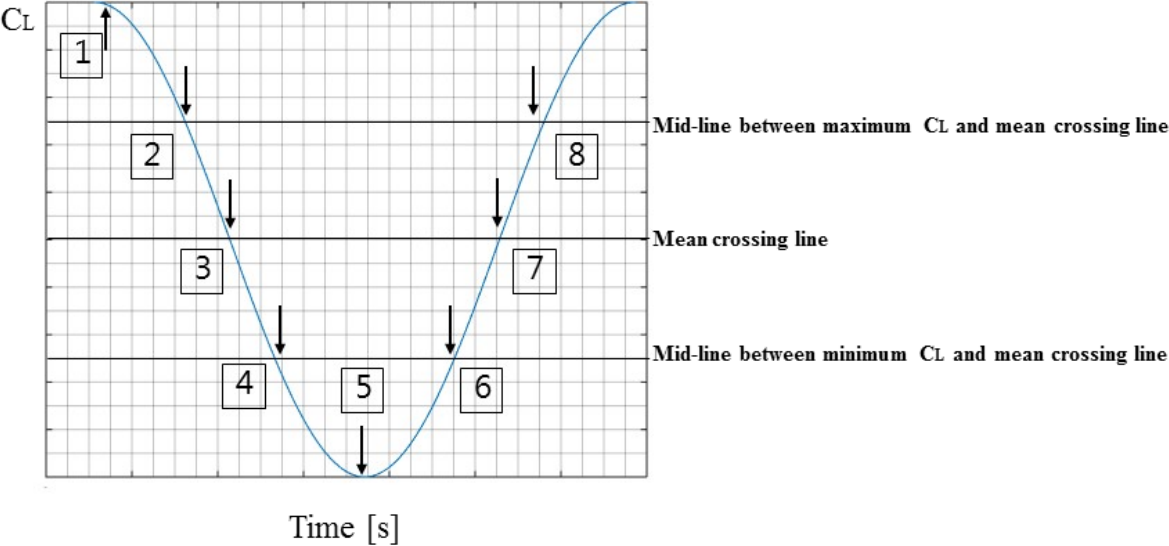
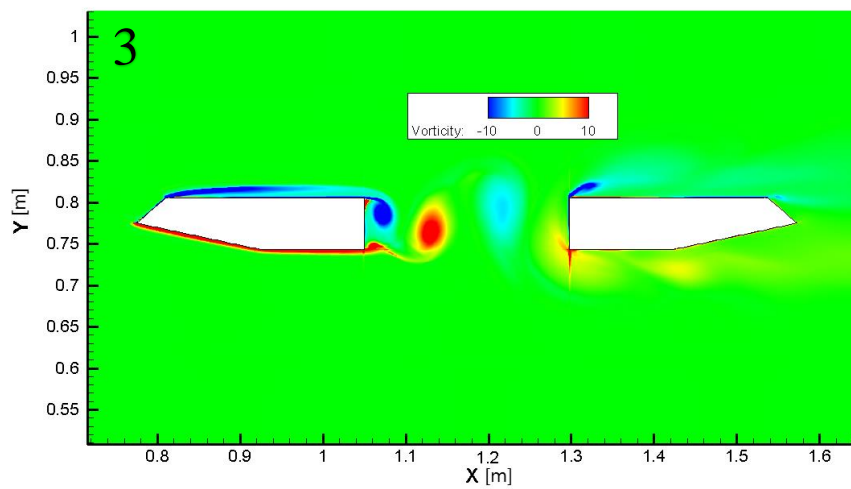
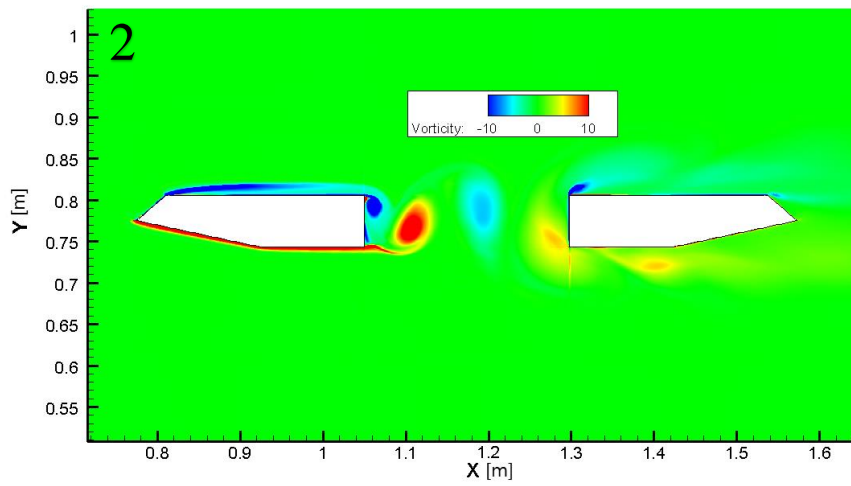
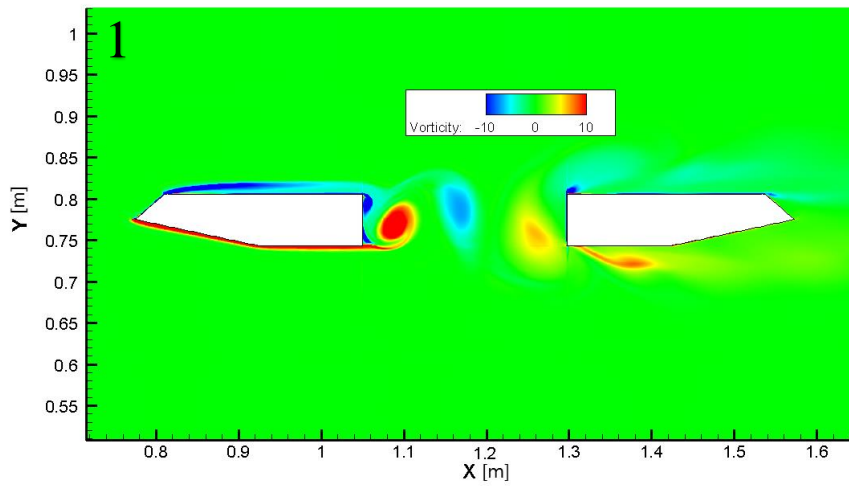
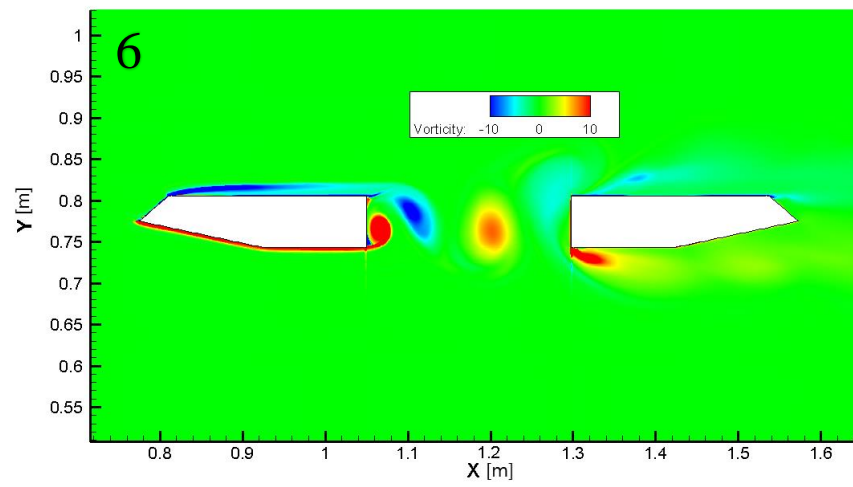
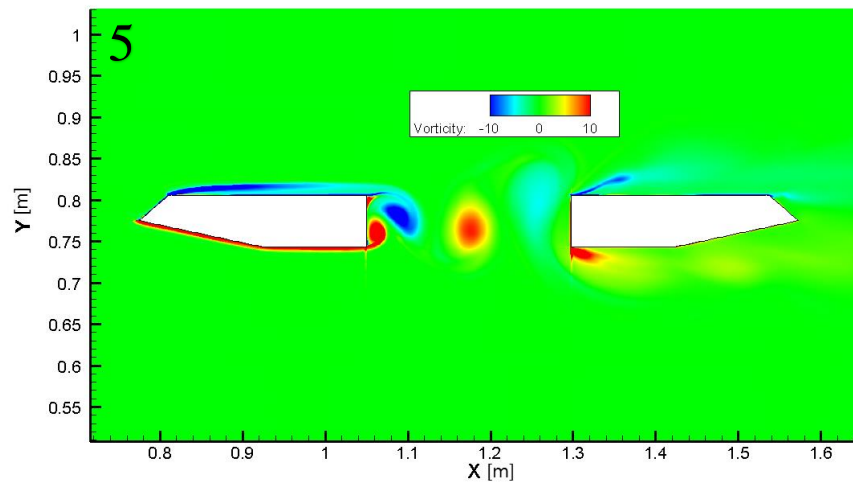
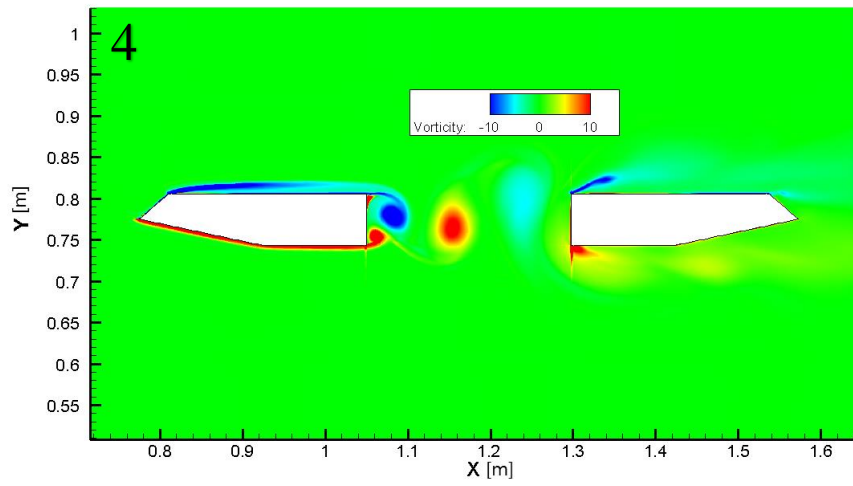


Figure 13: 8 Investigation time instances for the  $C_L$ (the sum of the two decks) variation in one period

Figure 14 shows vorticity plots for each investigation time instances of  $AoA + 0.1^\circ$  case. Note that the vorticity signs are assigned as right hands rule. Thus positive vorticity means counter clock-wise rotation, negative vorticity means clock-wise rotation. And the X value and Y value in the plots mean the coordinates in meter where the origin  $(x, y) = (0, 0)$  is left lower corner of the domain. See Figure 6 for the reference.







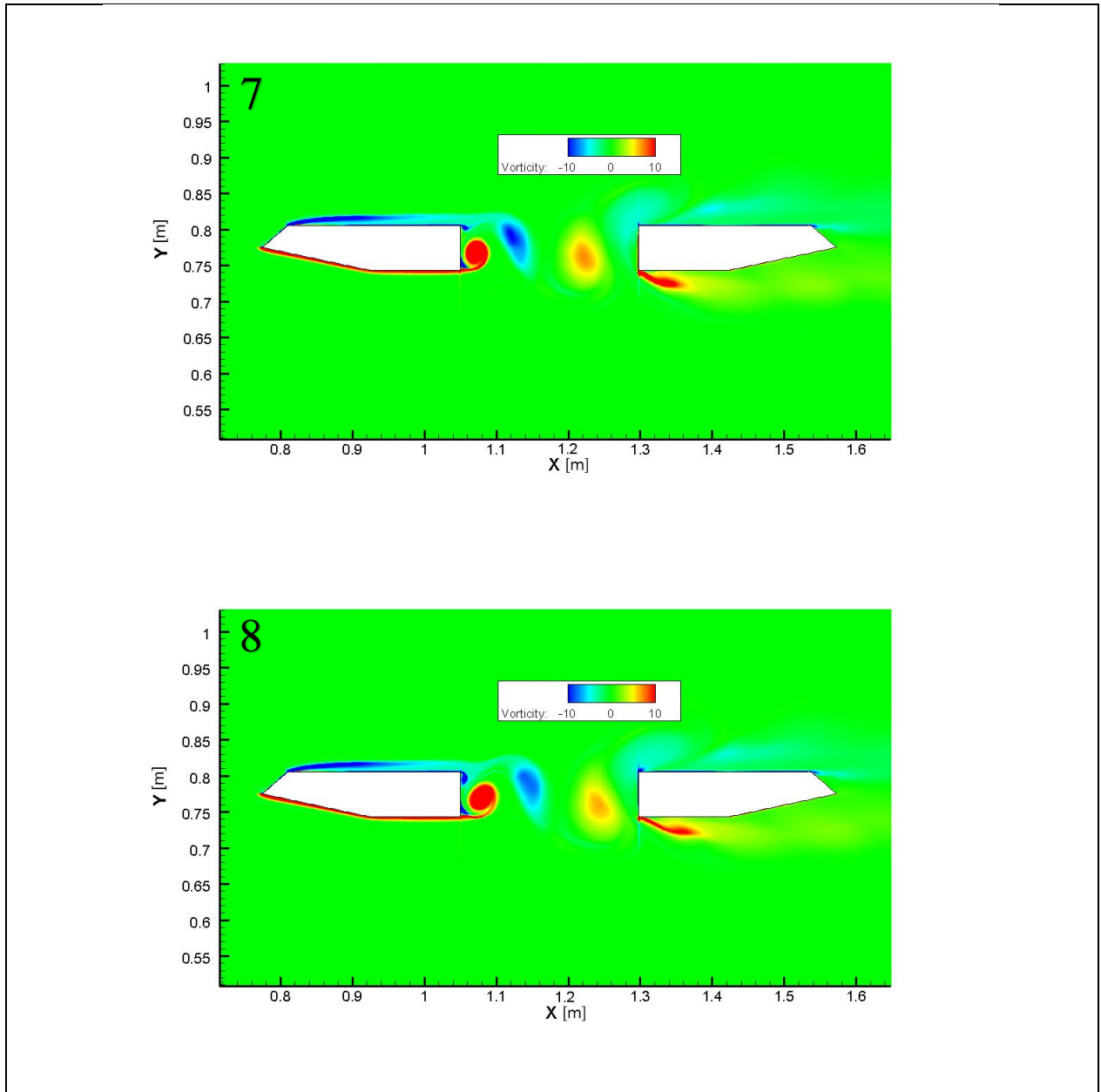


Figure 14: Vorticity contour plots from investigation point 1 to point 8 of angle of attack  $+ 0.1^\circ$  case

In the one period, it is observed that the vortices are generated from upper and lower edges at the downstream vertical edge of the windward deck and the vortices move to and attack to the leeward deck periodically. The sizes of upper and lower vortices are different due to the asymmetric geometry. The generation of these periodic vortices is the main reason of VIV.

It can be concluded that in case of  $AoA + 0.1^\circ$ , the main driver of VIV is the periodic asymmetric generation of the vortices. Thus, the design insights to reduce VIV can be found, such as geometry modification to reduce the separation of the flow, stabilizers to block the vortices against the attack and so on.

Similar flow characteristic can be observed in the range of AoA  $-6.2^\circ$  to AoA  $+4.4^\circ$ . In this range, the drag coefficient has two peaks, lift and moment coefficients have one peak per period. Figure 15 shows the aerodynamic coefficients plots for AoA  $+3.2^\circ$  case. Especially for the drag coefficient, the two peaks are different from that of AoA  $+0.1^\circ$  case. The two peaks have almost same height for AoA  $+0.1^\circ$  case and the two peaks heights are different in AoA  $+3.2^\circ$  case. In the range of AoA  $-6.2^\circ$  to AoA  $+4.4^\circ$ , the drag peak behavior is the main difference between the cases.

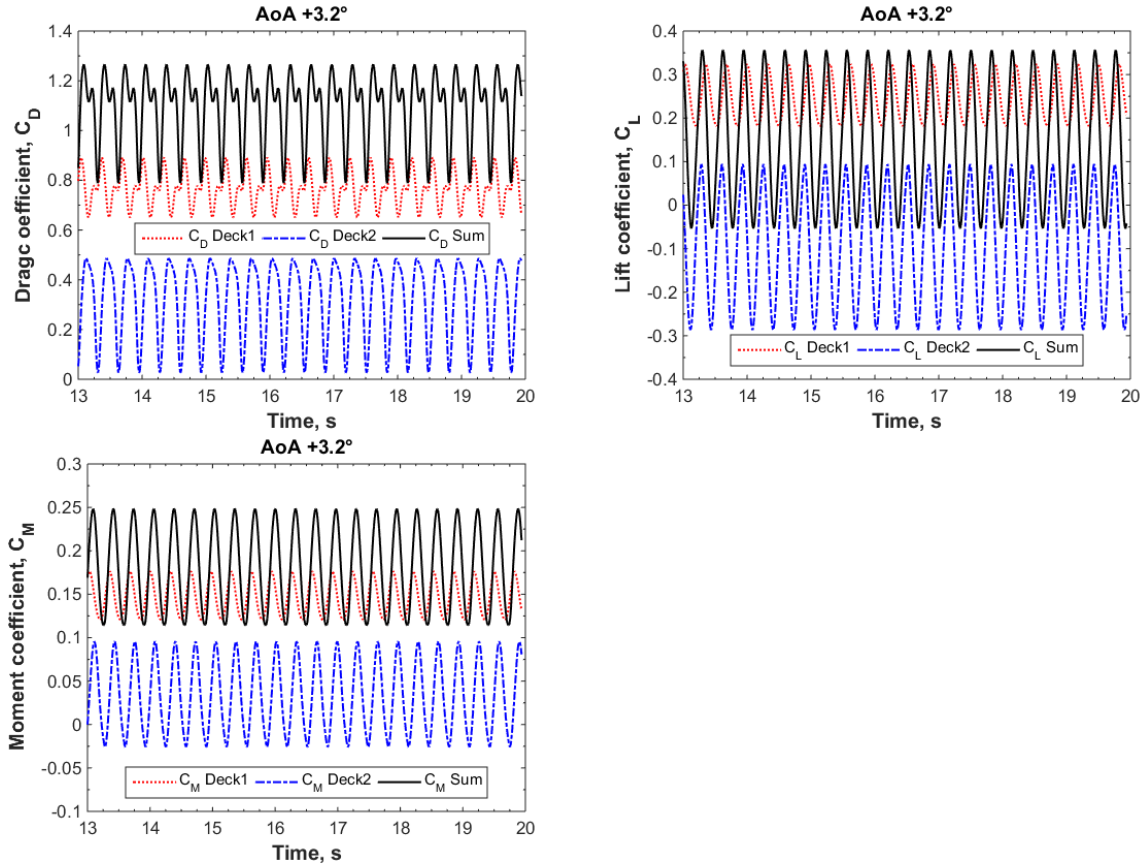


Figure 15: Drag, lift and moment coefficients for each bridge deck and the sum of decks of angle of attack  $+3.2^\circ$  case

AoA  $+6.3^\circ$  case is an important case where the flow characteristic begins to change. From AoA  $+6.3^\circ$  to AoA  $+10.2^\circ$ , there are no more double peaks in the drag coefficient. When the AoA is larger than  $+6.3^\circ$ , the vortices at the leeward deck that generated from the upper deck surface at the leeward deck and the tail edge begin to interact. From AoA  $+0.1^\circ$  to AoA  $+4.4^\circ$ , there is no interaction between the vortices. Figure 16 shows the drag, lift and moment coefficients plots for AoA  $+6.3^\circ$  case and Figure 17 shows the streamlines for AoA  $+6.3^\circ$  case. In Figure 16, it is shown that the flow characteristic has changed with respect to lower AoA cases, where no more double peaks in the drag coefficient. And also it can be seen in Figure 17 that the interaction exists between the vortices at the leeward deck.

At AoA  $+10.2^\circ$ , the vortices are joint to and it generates a big vortex at the leeward deck while at AoA  $+6.3^\circ$  the vortices interact without generating a big vortex. This changes of the flow characteristic can be studied with the function of the AoA. As AoA increases, the vortices which are generated at the upper surface of the leeward deck and at the tail edge getting bigger and when AoA reaches certain amplitude of AoA, in our case at AoA  $+6.3^\circ$ , the vortices begin to interact and merge.

Figure 18 shows streamline plot for AoA +10.2° case where a vortex at the upper surface of the windward deck and a big vortex at the leeward deck can be observed. From AoA +0.1° to AoA +6.3°, only a very small vortex exists at the upper surface of the windward deck. From AoA +8.1°, the vortex at the upper surface of the windward deck is getting bigger.

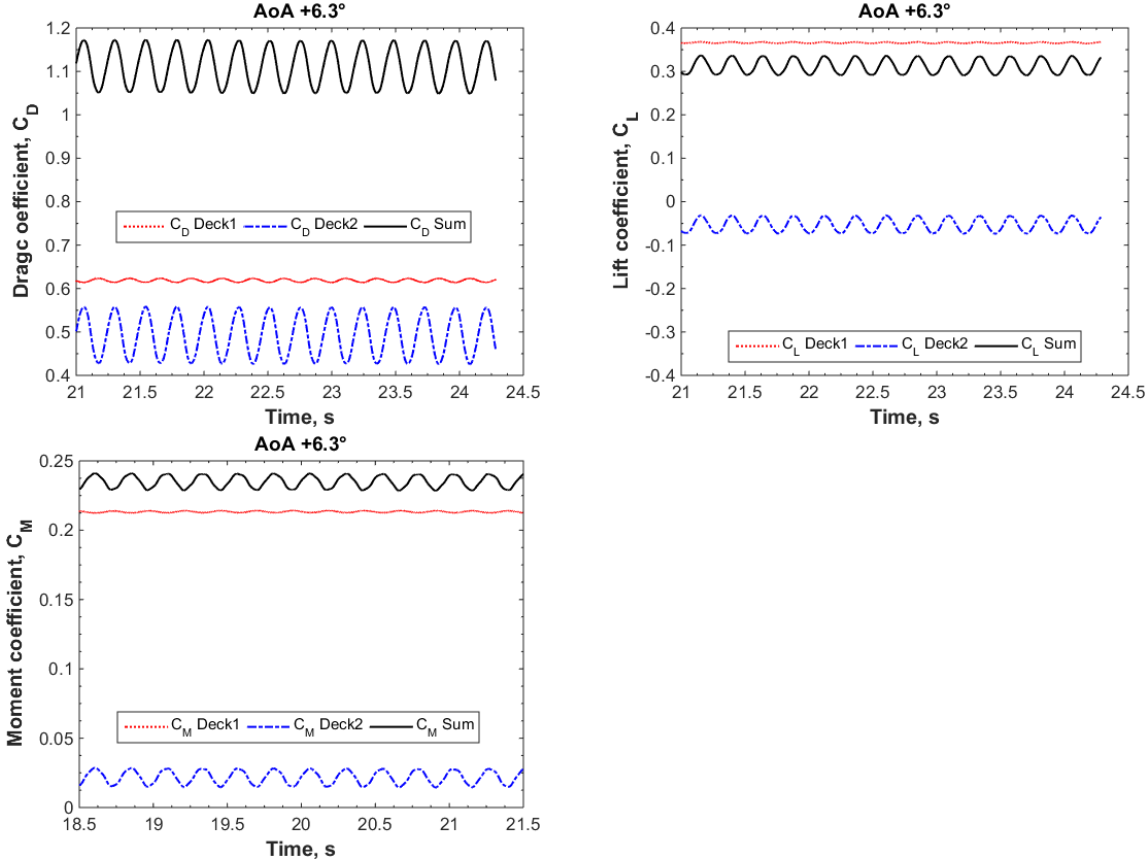


Figure 16: Drag, lift and moment coefficients for each bridge deck and the sum of decks of angle of attack +6.3° case

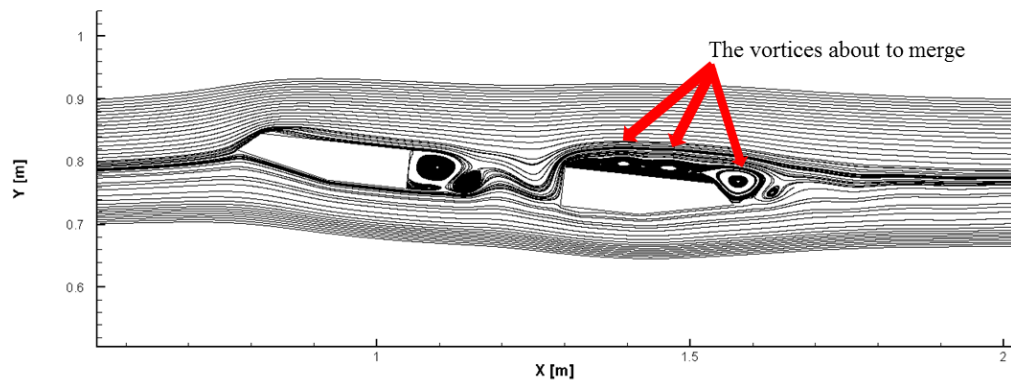
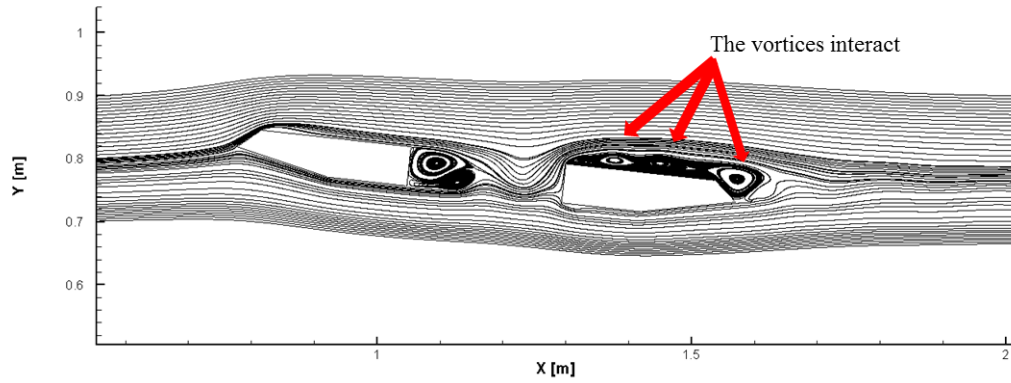


Figure 17: Streamlines of angle of attack  $+6.3^\circ$  case

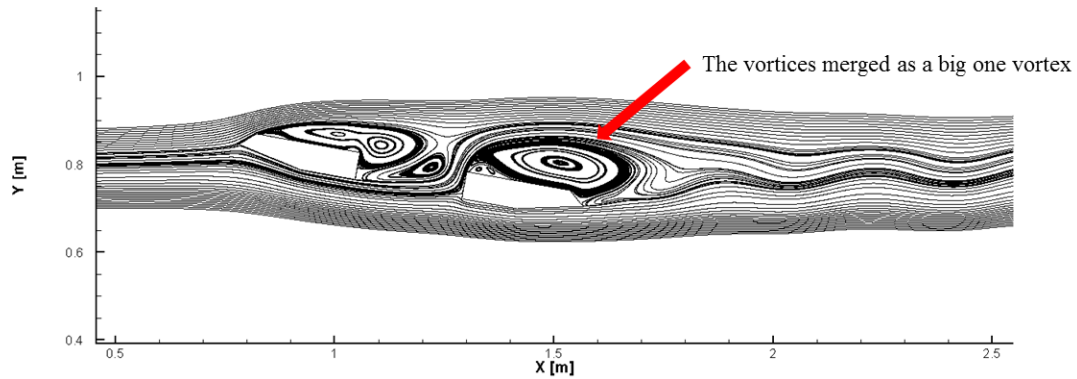


Figure 18: Streamline of angle of attack  $+10.2^\circ$  case

In negative AoA range from AoA  $-1.4^\circ$  to AoA  $-6.2^\circ$ , the drag coefficient has two peaks in one period while other coefficients have one peak per one period. From AoA  $-8.1^\circ$  the flow characteristic changes. The coefficients are chaotic as shown in Figure 19 while there are massive interactions between the vortices.

Figure 20 shows streamline plots for AoA  $-10.0^\circ$  case. At the lower surface of the leeward deck, a big vortex is generated then it is detached and regenerated over the time. The main difference between AoA  $+10.2^\circ$  and AoA  $-10.0^\circ$  is, at AoA  $+10.2^\circ$  the big vortex is almost stationary at the upper surface of the leeward deck while at AoA  $-10.0^\circ$  case, the big vortex is not stationary over the time. This complicated behavior of the vortex is the reason of the chaotic behavior of the parameters. Thus AoA  $-10.0^\circ$  is more critical region for the bridge, VIV reducing measures were tested at the lower surfaces of the decks (Hansen et al. (2016)) due to this reason.

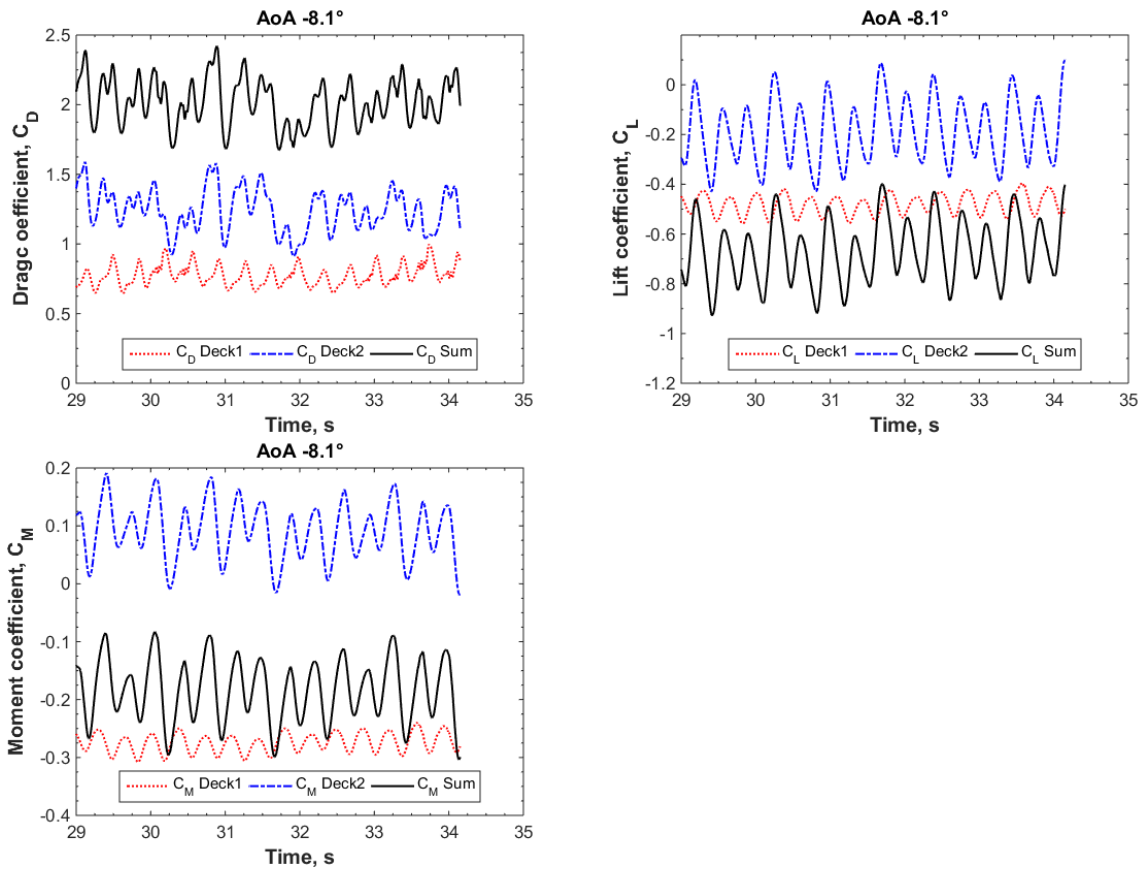


Figure 19: Drag, lift and moment coefficients for each bridge deck and the sum of decks of angle of attack  $-8.1^\circ$  case

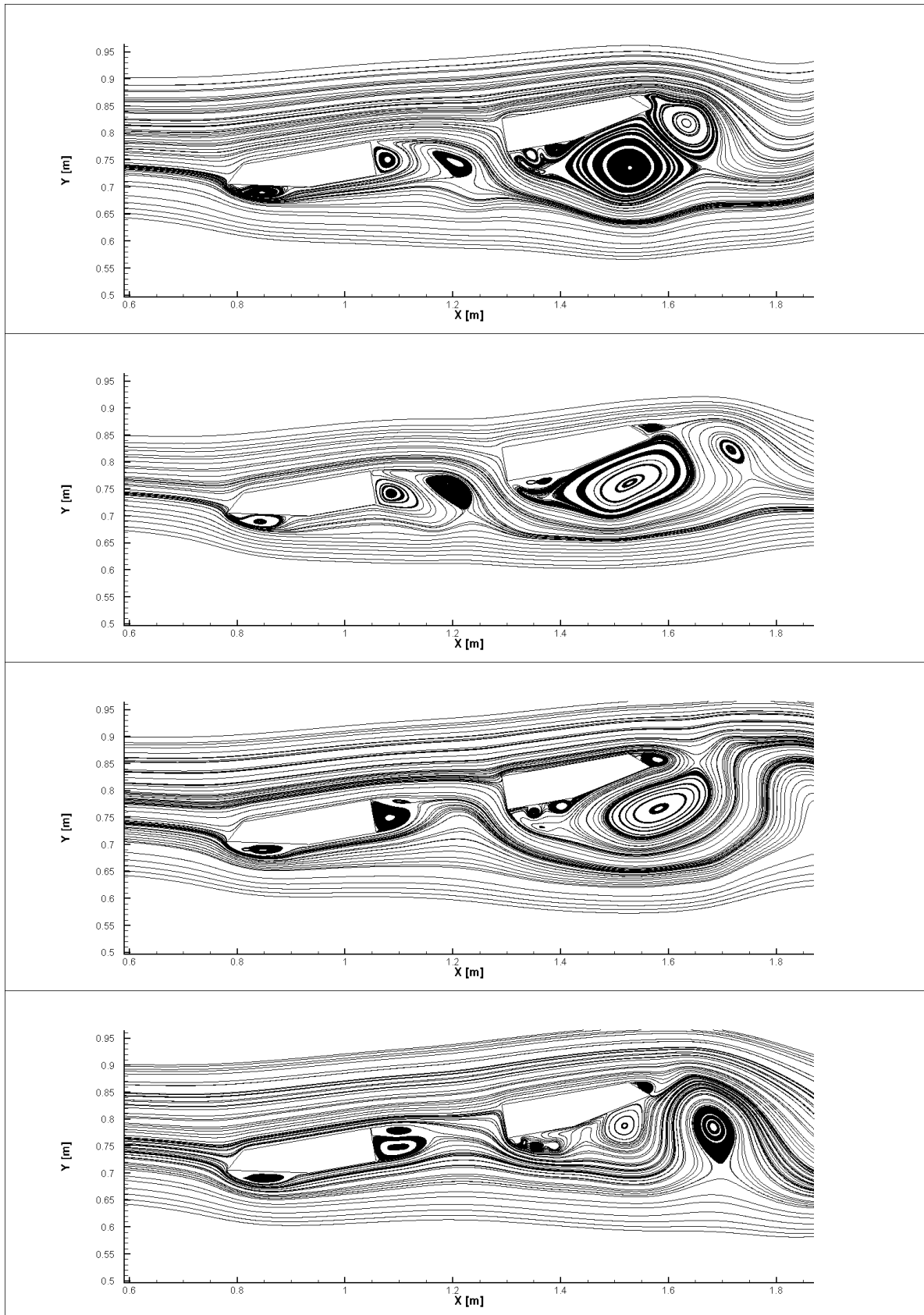


Figure 20: Instantaneous streamlines of angle of attack  $-10.0^\circ$  case

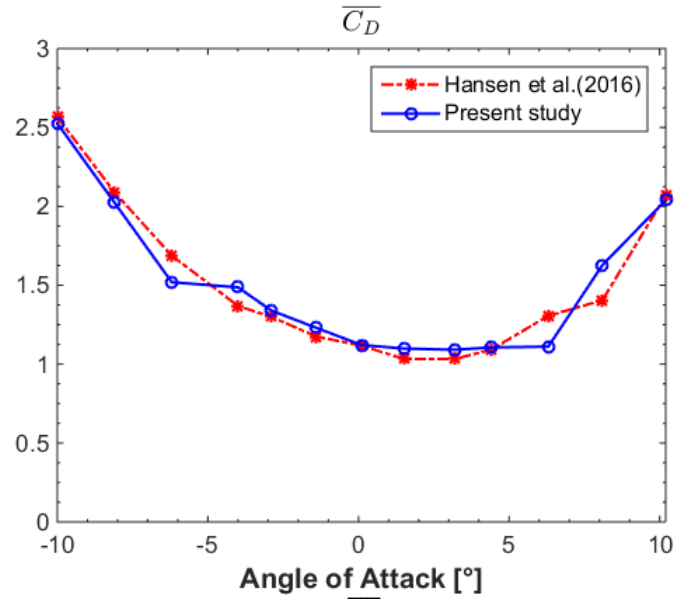


Figure 21: Variation of  $\overline{C_D}$  with angle of attack

Figure 21 shows the variation of the  $\overline{C_D}$  with AoA. The previous wind tunnel experimental study (Hansen et al. (2016)) and the present study results are shown. The present study results show a good agreement of the drag coefficient with the experimental results in all AoA range. In the present study, the drag coefficients are stable from AoA + 0.1° to AoA + 6.3° while in the experimental results, the drag coefficient starts to increase from AoA + 6.3°. Since AoA + 6.3° is the transient case where the flow structures and physics begin to change, there can be errors both in the present study and the experimental result. Deviations of the wind experimental results are required to validate.

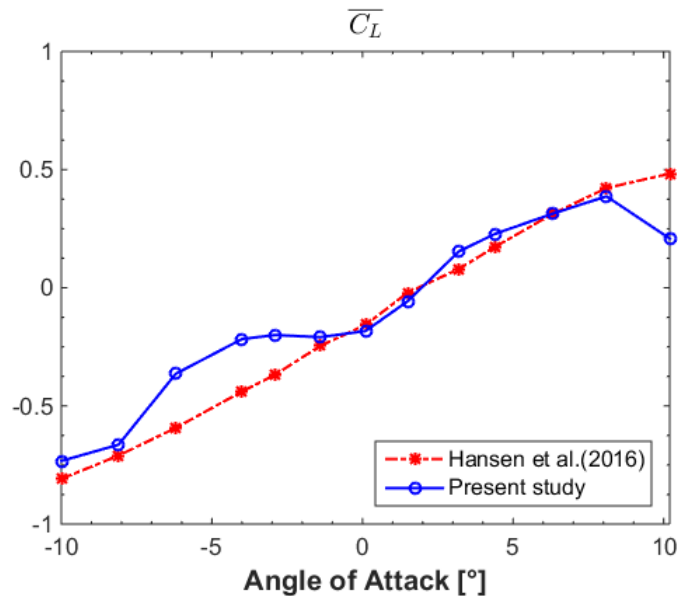


Figure 22: Variation of  $\overline{C_L}$  with angle of attack

Figure 22 shows  $\overline{C_L}$  versus AoA. It shows a good agreement of the lift coefficient with the experimental results in all AoA range except AoA + 10.2°. The abrupt drop of the lift coefficient is observed at AoA + 10.2°. It is considered that this is due to the turbulence modelling, which is not good enough to capture the flow structure in this case. As AoA increases, there are more accelerations over the decks which can cause too fast flow over the decks in the simulations than actual flow. The 3D flow effect is not considered in the present study, so here it can be concluded that the k- $\omega$  SST turbulence model has a limitation of estimating the parameters in high AoA where the high acceleration exists. This limitation



of the  $k-\omega$  SST turbulence model in high AoA is reported in Sánchez et al. (2015).

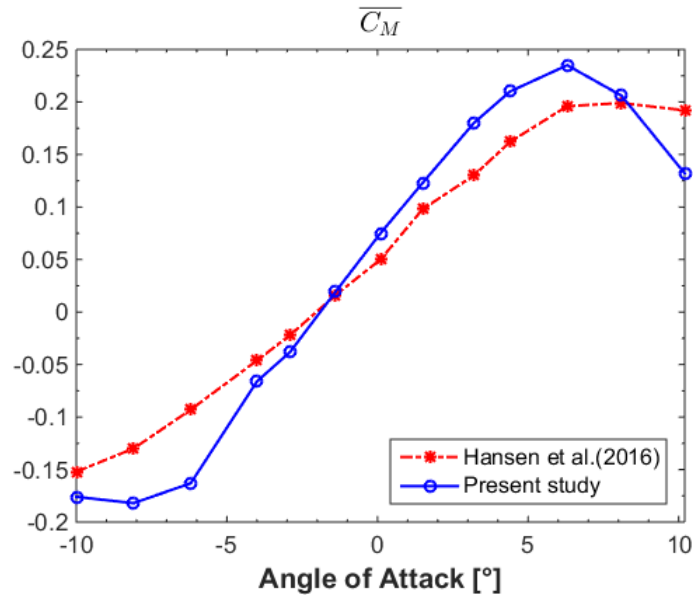


Figure 23: Variation of  $\overline{C_M}$  with angle of attack

Figure 23 shows  $\overline{C_M}$  versus AoA. It also shows a good agreement of the moment coefficient with the experimental results. The moment coefficient drop at AoA +10.2° is observed same as the lift coefficient at AoA +10.2°. The correlation factor of two data sets in the present study,  $C_L$  and  $C_M$ , is 0.97. This means the moment coefficient is dominated by the lift coefficient. So this explains the abrupt drop of both the lift coefficient and moment coefficient at AoA +10.2°. And the present study result results of  $C_M$  have slightly higher gradient than that of the experimental results, and the trend is similar as in the previous study by Nieto et al. (2008).

The previous publications (Diane et al., 2006; Sánchez et al., 2015; Nieto et al., 2008 and 2010; Laima and Li, 2015; Larsen et al., 2008; Vos, 2006) already reported that the  $k-\omega$  SST turbulence model is a good model for evaluating the flow around the bridge although there is a trend that over- or under-estimation of the coefficients at high AoA range.

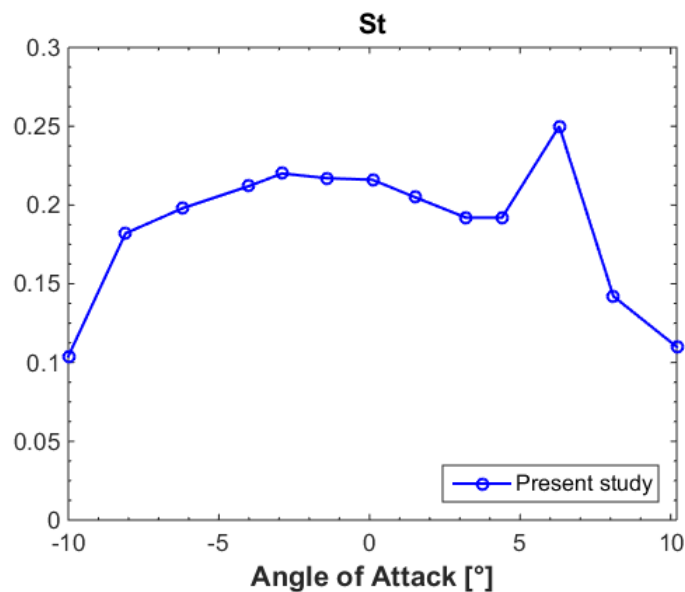


Figure 24 Variation of St with angle of attack

Figure 24 shows St number versus AoA. The predicted Strouhal numbers of the present study show that there is an abrupt increase at AoA + 6.3° and this is considered due to the flow structure change by the interaction of the vortices. In the range of AoA -8.1° to AoA +4.4°, the St numbers are in the range of 0.18 to 0.22, relatively stable. The St number increases at AoA + 6.3° to 0.250 and it decreases at AoA + 8.1° to 0.142 and +10.2° to 0.110 gradually. In the experimental report, St number for AoA + 0.1° case is reported as 0.160, but the test environments are different. The present study using same conditions that was used for the static coefficient test in the experiment, while the vortex induced vibration test was used for the St number calculation in the experiment. The main difference between the tests is the static coefficient test uses high turbulent inlet flow, where the turbulence intensity is larger than 10 %, while the vortex induced vibration test uses low turbulent flow with less than 1 % turbulence intensity (Hansen et al. (2016)). Additional experimental results are required to validate the St number study results.

Table 5 shows the contribution to  $C_D$  and  $C_L$  with standard deviations of each deck, and Figure 25 the contribution to  $C_D$  and  $C_L$  of each deck. Note that for the  $C_L$ , absolute values are considered.

As AoA increases from AoA + 0.1°, the contribution to  $C_D$  of the second deck also increases. The same trend can be seen as AoA decreases from AoA + 0.1°. While the contribution to  $C_L$  of the second deck is dominating factor at AoA + 0.1° and the deck contribution decreases as AoA increases. In the negative AoA range, the first deck contribution increases as AoA decreases.

CFD study can provide useful assessment tools like Table 5 and Figure 25 for the engineering design purposes. The experiment requires huge resources while CFD can provide reference information to understand the flow physics and insights to improve the design.

Table 5: The contribution to  $C_D$  and  $C_L$  with standard deviation of each deck

AoA (°)	$\overline{C_D, deck1}$	$\overline{C_D, deck2}$	$\overline{C_L, deck1}$	$\overline{C_L, deck2}$	$s_{C_D, deck1}$	$s_{C_D, deck2}$	$s_{C_L, deck1}$	$s_{C_L, deck2}$
0.1	0.9561	0.1688	-0.0032	-0.1752	0.0882	0.1889	0.0895	0.1353
1.5	0.9101	0.1884	0.0988	-0.1559	0.0989	0.1809	0.0776	0.1405
3.2	0.7698	0.3207	0.2465	-0.0922	0.0706	0.1571	0.0500	0.1311
4.4	0.7540	0.3521	0.3061	-0.0780	0.0633	0.1190	0.0424	0.1161
6.3	0.6188	0.4924	0.3663	-0.0532	0.0034	0.0465	0.0012	0.0147
8.1	0.8757	0.7519	0.3858	0.0014	0.0111	0.0512	0.0036	0.0468
10.2	1.0131	1.0261	0.2345	-0.0263	0.0462	0.1694	0.0226	0.0783
-1.4	1.0124	0.2171	-0.0740	-0.1350	0.0780	0.1556	0.0966	0.1358
-2.9	1.0087	0.3313	-0.1315	-0.0683	0.0769	0.1244	0.0957	0.1339
-4.0	0.9788	0.5084	-0.1664	-0.0502	0.0896	0.0934	0.0901	0.1319
-6.2	0.7666	0.7526	-0.3292	-0.0348	0.0542	0.0836	0.0641	0.1502
-8.1	0.7772	1.2457	-0.4805	-0.1838	0.0743	0.1526	0.0402	0.1268
-10.0	0.7822	1.7441	-0.5098	-0.2232	0.0786	0.2229	0.0686	0.0893

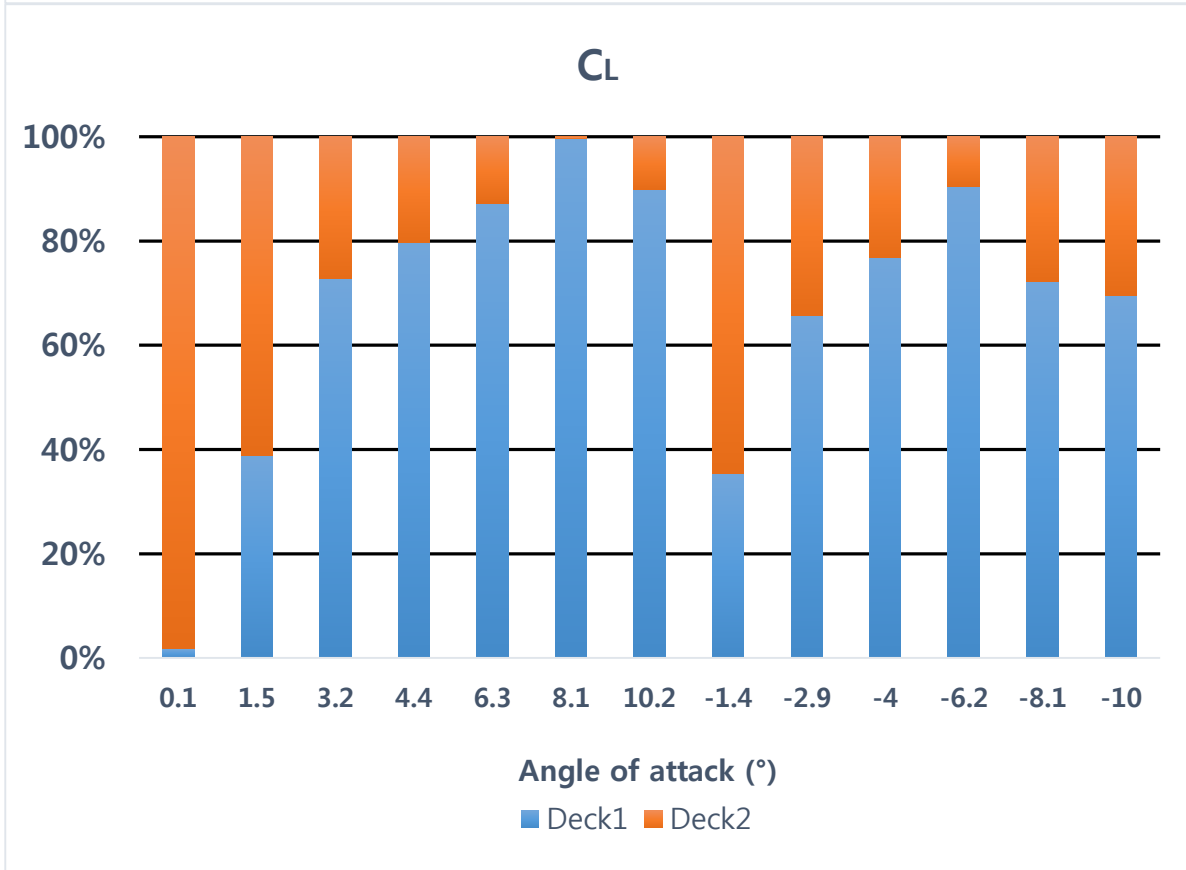
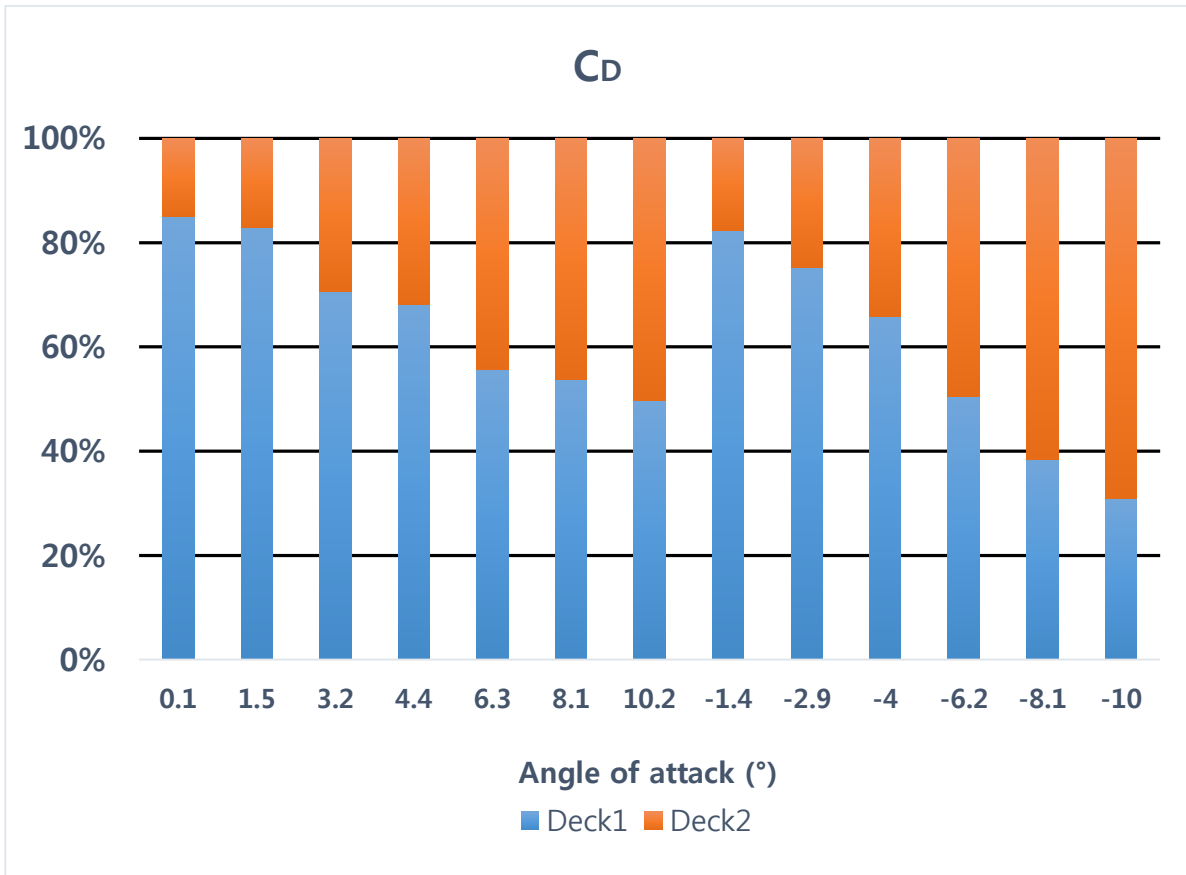


Figure 25: Variation of the contribution to  $C_D$  and  $C_L$  of each deck with angle of attack

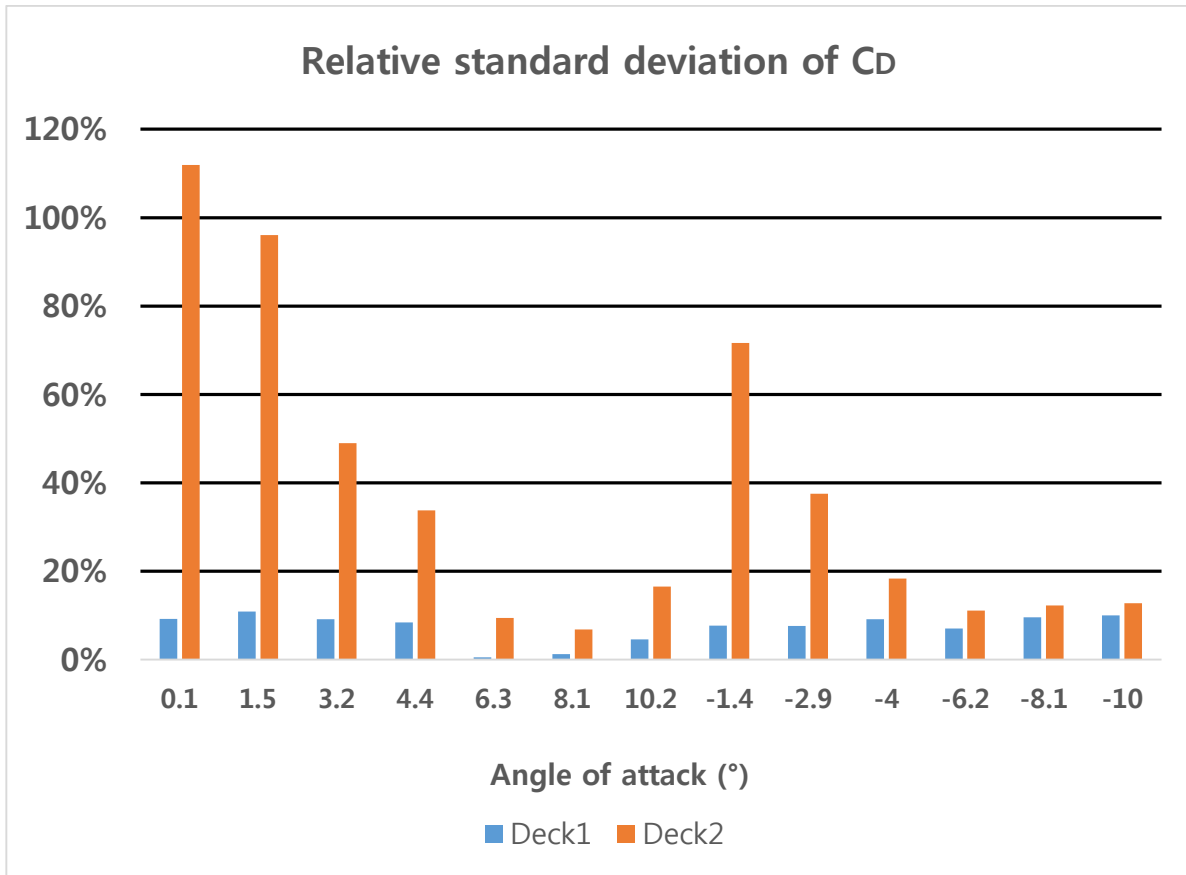


Figure 26: Variation of the relative standard deviation of  $C_D$  of each deck with angle of attack

Figure 26 shows the relative standard deviation (RSD) of  $C_D$ , where RSD is defined as  $RSD = \frac{s}{\bar{x}} \times 100\%$ , where  $s$  = standard deviation and  $\bar{x}$  = mean value, and Deck1 means the windward deck and Deck2 means the leeward deck. This parameter shows how much the fluctuation exists at each deck with respect to its average value, and helps us to understand the flow physics as function of AoA.

The windward deck has quite stable RSD values in all AoA range of RSD 5 % to 10 % while AoA +6.3° and AoA +8.1° cases have very low RSD values about RSD 1 %. Which means the drag coefficients at the windward deck are almost stable in these two cases. The leeward deck has much larger RSD values in all AoA range with respect to the windward deck, the values show the trend that the RSD values decrease as AoA increases. Since in the previous wind tunnel experimental test study (Hansen et al. (2016)), only average values are available, with other parameters this RSD parameter helps us to draw insights and to understand the flow physics.

For example, in Figure 25, the drag contributions to  $C_D$  of AoA +10.2° and AoA -10.2° are different. For AoA +10.2°, the contribution of each deck is almost 50:50 which means same drag force is applied to each deck, while for AoA -10.2° the contribution to  $C_D$  of the leeward deck is larger than twice times of the windward deck. Because at AoA +10.2° case the accelerated flow after the windward deck does not attack the leeward deck as shown in Figure 18, while at AoA -10.2° the accelerated flow after the windward deck hits the leeward deck as shown in Figure 20. This is the main reason of the contribution difference between the two cases. Thus it is concluded that the flow structures and physics of positive AoA and negative AoA are different. Also this explains why many configurations with VIV reducing measures under the decks were tested in the wind tunnel test, since the flow causes more force fluctuations on the bridge in the negative high AoA range.

## 7 Conclusion

2D CFD simulations of flow around a twin-box girder bridge at  $Re = 3.1 \cdot 10^4$  in the range of AoA -10.0° to AoA +10.2° have been performed. Mesh refinement analysis and time step sensitivity analysis were also conducted.

The present study results show a good agreement with the experimental results (Hansen et al. (2016)) in terms of  $C_D$ ,  $C_L$  and  $C_M$ .

The drag coefficient is less sensitive to mesh resolution, but the lift and the moment coefficients are more sensitive to both element numbers and meshing methodology.

The values and trends of the lift and moment coefficients show a good agreement with the experimental results, although the abrupt drop of the lift and moment coefficients are observed at AoA +10.2°.

The present study shows CFD approach to investigate the flow structures and physics around the bridge decks by capturing the 8 investigation points of one lift coefficient period of AoA + 0.1° case. This methodology can be applied to the other AoA cases.

The main goal of this study is: To verify if k- $\omega$  SST turbulence model is valid for the analysis of flow around the bridge has been checked with its limitation at high AoA range. The present study results show a good agreement in the range of AoA -10.0° to +10.2° in terms of  $C_D$ ,  $C_L$  and  $C_M$ , while there are lift and moment coefficients drop at AoA +10.2°. It is considered that the turbulence model is not good enough to capture the flow structure in this region due to the 3D effect of the flow.

In the meantime, the present study can be useful as an assessment tool for the engineering design purposes.

## 8 Further Work

Overall, the present 2D simulations with  $k-\omega$  SST turbulence model give satisfactory aerodynamic results compared with the experimental results for the low AoA range. For the high AoA, 3D LES, DES or DNS which are known to capture 3D flow structure well are recommended.

Also the Reynolds number effect can be studied through the present study by varying the Reynolds number.

For the Strouhal number, the experimental results are not available. And the wind tunnel test did not include deviations of test results which can be useful for the evaluation of validity of the present study. Further experimental and test results are required to validate.

## References

- Cengel, Y. A. and Cimbala, J. M. (2010). *Fluid Mechanics, Fundamentals and Applications*. McGraw-Hill, 2nd edition.
- Dahl, S. M. (2014). "Unsteady rans simulation of flow around rectangular cylinders with different aspect ratios at high Reynolds number." NTNU Master Thesis.
- Diana, G., Fiammenghi, G., Belloli, M. and Rocchi, D. (2006), "On the vortex shedding forcing on suspension bridge deck", *Journal of Wind Engineering & Industrial Aerodynamics* 94:341-363.
- Diana, G., Fiammenghi, G., Belloli, M. and Rocchi, D. (2013). "Wind tunnel tests and numerical approach for long span bridges: The Messina bridge." *Journal of Wind Engineering and Industrial Aerodynamics* 122: 38-49.
- European committee for standardization (2010). "EN 1991-1-4:2005 Eurocode 1: Actions on structures - Part 1-4: General actions -Wind actions."
- Ferziger, J. and Peric, M. (2002). *Computational Methods for Fluid Dynamics*. Springer, 3rd edition.
- Hansen, S. O., Horn, A. D. and Srouji, R. G. (2016). "Wind actions on cable-supported bridges." *Geotechnical & Structural Engineering Congress - Phoenix, Arizona*.
- Hansen, S. O., Srouji, R. G., Isaksen, B. and Berntsen, K. (2015). "Vortex-induced vibrations of streamlined single box girder bridge decks." *14th International Conference on Wind Engineering*.
- Hansen, S. O., Srouji, R. G. and Rasmussen, J. T. (2016). "Julsundet and Halsafjorden bridges Part II: Suspension bridge crossing Halsafjorden, Flutter and vortex-induced vibrations of a sharp-edged cross section." *Project Report*.
- Holmemo, M. (2015). "The effect of computational domain and Reynolds number on the flow around a 5:1 rectangular cylinder." *NTNU Project Thesis*.
- Homann, K., Rasmussen, J. T., Hansen, S. O., Reiso, M., Isaksen, B. and Aasland, T. A. (2016). "The use of wind tunnel facilities to estimate hydrodynamic data." *The European Physical Journal Conferences* 114.
- Kwok, K. C. S., Qin, X. R., Fok, C. H. and Hitchcock, P.A. (2012). "Wind-induced pressures around a sectional twin-deck bridge model: Effects of gap-width on the aerodynamic forces and vortex shedding mechanisms." *Journal of Wind Engineering and Industrial Aerodynamics* 110: 50-61.
- Laima, S. and Li, H. (2015). "Effects of gap width on flow motions around twin-box girders and vortex-induced vibrations." *Journal of Wind Engineering and Industrial Aerodynamics* 139: 37-49.
- Larsen, A., Savage, M., Lafrenière, A., Hui, M. C. H. and Larsen, S. V. (2008). "Investigation of vortex response of a twin box bridge section at high and low Reynolds numbers." *Journal of Wind Engineering and Industrial Aerodynamics* 96(6-7): 934-944.
- Launder, B. and Spalding, D. (1974). "The numerical computation of turbulent flows." *Computer Methods in Applied Mechanics and Engineering* 3:269–289.

- Li, H., Laima, S., Zhang, Q., Li, N. and Liu, Z. (2014). "Field monitoring and validation of vortex-induced vibrations of a long-span suspension bridge." *Journal of Wind Engineering and Industrial Aerodynamics* 124: 54-67.
- Mavriplis, D.J. (1996), "Mesh Generation and adaptivity for complex geometries and flows", *Handbook of Computational Fluid Mechanics*, Academic press.
- Menter, F. R. (1994), "Two-equation eddy-viscosity turbulence models for engineering applications", *American Institute of Aeronautics and Astronautics Journal* 32(8):1598-1605.
- Nieto, F., Hernández, S., Jurado, J. Á. and Baldomir, A., (2010), "CFD practical application in conceptual design of a 425 m cable-stayed bridge". *Wind and Structures* 13(4):309-326.
- Nieto, F., Zasso, A., Rocchi, D. and Hernandez S., (2008), "CFD verification of aerodynamic devices performance for the Messina Strait bridge", *Bluff Bodies Aerodynamics & Applications 6<sup>th</sup> international colloquium*.
- Nymo, D. A. (2015). "Numerical simulation of flow around two rectangular cylinders in tandem." NTNU Project Thesis.
- Ogawa, K., Shimodoi, H. and Oryu, T. (2002), "Aerodynamic characteristics of a 2-box girder section adaptable for a super-long span suspension bridge", *Journal of Wind Engineering & Industrial Aerodynamics* 90: 2033-2043.
- Ong, M. C. (2012). "Unsteady rans simulation of flow around a 5:1 rectangular cylinder at high Reynolds numbers." *Proceedings of the ASME 2012 31st International Conference on Ocean, Offshore and Arctic Engineering*.
- Qin, X. R., Kwok, K. C. S., Fok, C. H., Hitchcock, P. A. and Xu, Y. L. (2007), "Wind-induced self-excited vibrations of a twin-deck bridge and the effects of gap-width", *Wind and Structures* 10(5): 463-479.
- Qin, X. R., Kwok, K. C. S., Fok, C. H. and Hitchcock, P. A (2009), "Effects of frequency ratio on bridge aerodynamics determined by free-decay sectional model tests", *Wind and Structures* 12(5): 413-424.
- Rodi, W. (1993). *Turbulence models and their application in hydraulics: A state-of-the-art review*. A.A.Balkema, 3rd edition.
- Sánchez, R., Nieto, F., Kwok, K. C. S. and Hernández, S. (2015), "CFD analysis of the aerodynamic response of a twin-box deck considering different gap widths." *Congresso de Métodos Numéricos em Engenharia* 2015.
- Schewe, G. and Larsen, A., (1998), "Reynolds number effects in the flow around a bluff bridge deck cross section", *Journal of Wind Engineering & Industrial Aerodynamics* 74-76: 829-838.
- Schmitt, F.G., (2007), "About Boussinesq's turbulent viscosity hypothesis: historical remarks and a direct evaluation of its validity", *Comptes Rendus Mécanique* 335 ((9-10)): 617-627.
- Tian, X., Ong, M. C., Yang, J. and Myrhaug, D., (2013), "Unsteady RANS simulations of flow around rectangular cylinder with different aspect ratios", *Ocean Engineering* 58: 208-216.
- Vos, W. G. M. W. (2006). "The verification and validation of preliminary CFD results for the construction of an a priori aerodynamic model." *Delft University of Technology Master Thesis*.



Yang, Y., Ma, T. and Ge, Y. (2014). "Full scale measurement on structural dynamic characteristics and vortex-induced vibrations of a long-span suspension bridge." *Advances in Civil, Environmental, and Materials Research (ACEM14)*.

# Appendix

## A MATLAB code for the calculation of $C_D$ , $C_L$ , $C_M$ and $St$

```
close all; %close all figures
clear all; %clear workspace

tstart=0;% stabilized time. only data after this time will be used for
calculation
tend=0;
delta_t=0.00002;% time step, used for strouhal number calculation

%%Read file for deck1
fid=fopen('forceCoeffs.dat','r');
datacell=textscan(fid,'%f %f %f %f %f %f','HeaderLines',20);
fclose(fid);

data.t=datacell{1}; % read time data
data.cm=datacell{2}/(0.55^2); %read momentum coefficient data, cm
data.cl=datacell{4}/0.275/2; % read lift coefficient data, cl
data.cd=datacell{3}/0.0625; % read drag coefficient data, cd
data.length=0; %define data length, will be updated with stabilized data
length

%%Create new arrays of stable data
for i=1:length(data.cl)
if data.t(i)>=tstart % the data after stabilized time data will be
reconstructed as new array
data.length=data.length+1;
clstab(data.length)=data.cl(i);%Array for cl
cmstab(data.length)=data.cm(i);%Array for cm
cdstab(data.length)=data.cd(i);%Array for cd
end
end

%%Read file for deck2
fid=fopen('forceCoeffs2.dat','r');
datacell=textscan(fid,'%f %f %f %f %f %f','HeaderLines',20);
fclose(fid);

data.t1=datacell{1};
data.cm1=datacell{2}/(0.55^2);
data.cl1=datacell{4}/0.275/2;
data.cd1=datacell{3}/0.0625;
data.length1=0;

for i=1:length(data.cl1)
if data.t(i)>=tstart
data.length1=data.length1+1;
clstab1(data.length1)=data.cl1(i);
cmstab1(data.length1)=data.cm1(i);
cdstab1(data.length1)=data.cd1(i);
end
end

%%Findcd
[cdpeaks, locd]=findpeaks(cdstab,'MinPeakDistance',200,'MINPEAKHEIGHT',mean(cdstab));
```

```

cd=mean(cdstab(locd(1):locd(end)));
%%Findcm
[cmpeaks, locm]=findpeaks(cmstab, 'MinPeakDistance', 200, 'MINPEAKHEIGHT', mean(cmstab));
cm=mean(cmstab(locm(1):locm(end)));
%%Findcl
[clpeaks, locl]=findpeaks(clstab, 'MinPeakDistance', 400, 'MINPEAKHEIGHT', mean(clstab));
cl=mean(clstab(locl(1):locl(end)));

%%Findcd1
[cdpeaks1, locd1]=findpeaks(cdstab1, 'MinPeakDistance', 200, 'MINPEAKHEIGHT', mean(cdstab1));
cd1=mean(cdstab1(locd1(1):locd1(end)));
%%Findcm1
[cmpeaks1, locm1]=findpeaks(cmstab1, 'MinPeakDistance', 200, 'MINPEAKHEIGHT', mean(cmstab1));
cm1=mean(cmstab1(locm1(1):locm1(end)));
%%Findcl1
[clpeaks1, locl1]=findpeaks(clstab1, 'MinPeakDistance', 400, 'MINPEAKHEIGHT', mean(clstab1));
cl1=mean(clstab1(locl1(1):locl1(end)));

%%Fast fourier tranform to find Strouhal number
Fs=1/delta_t; % Frequency
clsum=clstab+clstab1;
Y=fft(clsum); %FFT for combined lift coefficient
Y=abs(Y);
L=length(Y);
f = Fs*(0:(L/2))/L;
P2 = abs(Y/L);
P1 = P2(1:L/2+1);
P1(2:end-1) = 2*P1(2:end-1);
[pxxpeak, locpxx]=findpeaks(Y, 'MinPeakDistance', length(Y)/10);
St1=f(locpxx(1))*0.0625/1;% The value for reduced frequency at the peak

%Display results
disp('Cd= ');
disp(cd+cd1);
disp('Cl= ');
disp(cl+cl1);
disp('Cm= ');
disp(cm+cm1);
disp('St1= ');
disp(St1);

%plot for cd
figure(1)
plot(data.t, data.cd, ':r', data.t, data.cd1, '-.b', data.t, data.cd+data.cd1, '-k', 'LineWidth', 1.5);
set(gca, 'Box', 'on', 'XMinorTick', 'on', 'YMinorTick', 'on')
xlabel('Time, s', 'fontSize', 15, 'fontWeight', 'bold')
ylabel('Drag coefficient, C_D', 'fontSize', 15, 'fontWeight', 'bold')
legend('C_D Deck1', 'C_D Deck2', 'C_D Sum', 'Location', 'south', 'Orientation', 'horizontal')
set(gca, 'fontsize', 13)
title('AoA +0.1')
hold on

%plot for cl

```

```

figure(2)
plot(data.t,data.cl,':r',data.t,data.c11,'-.b',data.t,data.cl+data.c11,'-
k','LineWidth',1.5);
set(gca,'Box','on','XMinorTick','on','YMinorTick','on')
xlabel('Time, s','fontSize',15,'fontWeight','bold')
ylabel('Lift coefficient, C_L','fontSize',15,'fontWeight','bold')
legend('C_L Deck1','C_L Deck2','C_L
Sum','Location','south','Orientation','horizontal')
set(gca,'fontSize',13)
title('AoA +0.1')
hold on

%plot for st
figure(3)
plot(f*0.0625/1,P1,'k')
set(gca,'Box','on','XMinorTick','on','YMinorTick','on')
xlabel('Reduced Frequency (fD/U)','fontSize',15,'fontWeight','bold')
ylabel('Amplitude','fontSize',15,'fontWeight','bold')
title('FFT for C_L Sum')
set(gca,'fontSize',13)
hold on

%plot for cm
figure(4)
plot(data.t,data.cm,':r',data.t,data.c11,'-.b',data.t,data.cm+data.c11,'-
k','LineWidth',1.5);
set(gca,'Box','on','XMinorTick','on','YMinorTick','on')
xlabel('Time, s','fontSize',15,'fontWeight','bold')
ylabel('Moment coefficient, C_M','fontSize',15,'fontWeight','bold')
legend('C_M Deck1','C_M Deck2','C_M
Sum','Location','south','Orientation','horizontal')
set(gca,'fontSize',13)
title('AoA +0.1')
hold on

```

## B OPENFOAM System files

### B-1 fvSchemes

```

/*-----*- C++ -*-----*\
|=====|
|\ \ / F ield | OpenFOAM: The Open Source CFD Toolbox |
|\ \ / O peration | Version: 1.6 |
|\ \ / A nd | Web: http://www.OpenFOAM.org |
|\ \ M anipulation |
\*-----*/
FoamFile
{
    version 2.0;
    format ascii;
    class dictionary;
    object fvSchemes;
}
// ***** //

ddtSchemes

```

```

{
default   CrankNicolson 0.5;
}

gradSchemes
{
  default   Gauss linear;
  grad(p)   Gauss linear;
  grad(U)   Gauss linear;
}

divSchemes
{
  default   none;
  div(phi,U)   Gauss limitedLinearV 1;
  div(phi,k)   Gauss limitedLinear 1;
  div(phi,epsilon) Gauss limitedLinear 1;
  div(phi,omega) Gauss limitedLinear 1;
  div(phi,R)   Gauss limitedLinear 1;
  div(R)       Gauss linear;
  div(phi,nuTilda) Gauss limitedLinear 1;
  div((nuEff*dev2(T(grad(U)))) Gauss linear;
}

laplacianSchemes
{
  default   none;
  laplacian(nuEff,U) Gauss linear corrected;
  laplacian((1|A(U)),p) Gauss linear corrected;
  laplacian(DkEff,k) Gauss linear corrected;
  laplacian(DepsilonEff,epsilon) Gauss linear corrected;
  laplacian(DomegaEff,omega) Gauss linear corrected;
  laplacian(DREff,R) Gauss linear corrected;
  laplacian(yPsi) Gauss linear corrected;
  laplacian(DnuTildaEff,nuTilda) Gauss linear corrected;
}

wallDist
{
method meshWave;
}

interpolationSchemes
{
  default   linear;
  interpolate(U) linear;
}

snGradSchemes
{
  default   corrected;
}

fluxRequired
{

```

```

default    no;
p          ;
}

// *****

```

## B-2 fvSolution

```

/*----- C++ -----*\
|=====| |=====|
|\ \ / F i e l d | OpenFOAM: The Open Source CFD Toolbox |
|\ \ / O p e r a t i o n | Version: 1.6 |
| \ \ / A n d | Web: www.OpenFOAM.org |
| \ \ M a n i p u l a t i o n | |
\*-----*/
FoamFile
{
  version 2.0;
  format  ascii;
  class  dictionary;
  location "system";
  object  fvSolution;
}
// *****

solvers
{
  p
  {
    solver      PCG;
    preconditioner DIC;
    tolerance   1e-06;
    relTol      0;
  }

  pFinal
  {
    solver      PCG;
    preconditioner DIC;
    tolerance   1e-06;
    relTol      0;
  }

  U
  {
    solver      PBiCG;
    preconditioner DILU;
    tolerance   1e-05;
    relTol      0;
  }

  k
  {
    solver      PBiCG;
    preconditioner DILU;
  }
}

```

```

    tolerance    1e-05;
    relTol      0;
}

epsilon
{
    solver      PBiCG;
    preconditioner DILU;
    tolerance    1e-05;
    relTol      0;
}

omega
{
    solver      PBiCG;
    preconditioner DILU;
    tolerance    1e-05;
    relTol      0;
}

R
{
    solver      PBiCG;
    preconditioner DILU;
    tolerance    1e-05;
    relTol      0;
}

nuTilda
{
    solver      PBiCG;
    preconditioner DILU;
    tolerance    1e-05;
    relTol      0;
}

}

PISO
{
    nCorrectors    2;
    nNonOrthogonalCorrectors 3;
}

// ***** //

```

### B-3 controlDict

```

/*-----* C++ *-----*\
|=====|
|\ \ / F i e l d | OpenFOAM: The Open Source CFD Toolbox |
|\ \ / O p e r a t i o n | Version: 1.6 |
| \ \ / A n d | Web: www.OpenFOAM.org |
| \ \ M a n i p u l a t i o n |
\*-----*/

```

```

FoamFile
{
  version 2.0;
  format  ascii;
  class   dictionary;
  location "system";
  object  controlDict;
}
// ***** //

application  pisoFoam;

startFrom    latestTime;

startTime    0;

stopAt       endTime;

endTime      600;

deltaT       0.00005;

writeControl adjustableRunTime;

writeInterval 1;

purgeWrite   0;

writeFormat  ascii;

writePrecision 6;

writeCompression compressed;

timeFormat   general;

timePrecision 6;

functions
(
  forcesBridge1
  {
    type forces;
    functionObjectLibs ("libforces.so"); //Lib to load
    patches (bridge1);
    pName  p;
    UName  U;
    log false;
    rhoName rhoInf;
    rhoInf 1.225; //Reference density for fluid
    CofR (1.17375 0.775 0.5);
    outputControl timeStep;
  }
)

```



```

outputInterval 1;
}
forcesBridge2
{
type forces;
functionObjectLibs ("libforces.so"); //Lib to load
patches (bridge2);
pName p;
UName U;
log false;
rhoName rhoInf;
rhoInf 1.225; //Reference density for fluid
CofR (1.17375 0.775 0.5);
outputControl timeStep;
outputInterval 1;
}
forceCoeffsA
{
type forceCoeffs;
functionObjectLibs ("libforces.so");
outputControl timeStep;
outputInterval 1;
patches (bridge1);
pName p;
UName U;
log false;
rhoName rhoInf;
rhoInf 1.225;
CofR (1.17375 0.775 0.5);
liftDir (0 1 0);
dragDir (1 0 0);
pitchAxis (0 0 1);
magUInf 0.1; //reference velocity
lRef 1;
Aref 1;
}
forceCoeffsB
{
type forceCoeffs;
functionObjectLibs ("libforces.so");
outputControl timeStep;
outputInterval 1;
patches (bridge2);
pName p;
UName U;
log false;
rhoName rhoInf;
rhoInf 1.225;
CofR (1.17375 0.775 0.5);
liftDir (0 1 0);
dragDir (1 0 0);
pitchAxis (0 0 1);
magUInf 0.1;
lRef 1;
}

```

```

    Aref 1;
    }
    fieldAverage1
{
type      fieldAverage;
functionObjectLibs ( "libfieldFunctionObjects.so" );
enabled    true;
outputControl  outputTime;

fields
(
    U
    {
        mean    on;
        prime2Mean on;
        base    time;
    }

    p
    {
        mean    on;
        prime2Mean on;
        base    time;
    }
);
}

);
//

// ***** //

```